Optical Imaging of the Nanoscale Structure and Dynamics of Biological Membranes

Chamari S. Wijesooriya,[1] Charles K. A. Nyamekye,[1,2] Emily A. Smith[1,2,*]

[1] Department of Chemistry, Iowa State University, Ames, Iowa 50011 USA
[2] The Ames Laboratory, U.S. Department of Energy, Ames, Iowa 50011 USA

1. Introduction

Biological membranes serve as the fundamental unit of life, allowing the compartmentalization of cellular contents into subunits with specific functions. The bilayer structure, consisting of lipids, proteins, small molecules and sugars, also serves many other complex functions in addition to maintaining the relative stability of the inner compartments. Signal transduction, regulation of solute exchange, active transport, and energy transduction through ion gradients all take place at biological membranes, primarily with the assistance of membrane proteins. For these functions, membrane structure is often critical. The fluid-mosaic model introduced by Singer and Nicolson in 1972 evokes the dynamic and fluid nature of biological membranes.[1] According to this model, integral and peripheral proteins are oriented in a viscous phospholipid bilayer. Both proteins and lipids can diffuse laterally through the two-dimensional structure. Modern experimental evidence has shown, however, that the structure of the membrane is considerably more complex; various domains in the biological membranes, such as lipid rafts and confinement regions, form a more complicated molecular organization. The proper organization and dynamics of the membrane components are critical for the function of the entire cell. For example, cell signaling is often initiated at biological membranes and requires receptors to diffuse and assemble into complexes and clusters, and the resulting downstream events have consequences throughout the cell. Revealing the molecular level details of these signaling events is the foundation to understanding numerous unsolved questions regarding cellular life.

Optical imaging methods have substantial utility in revealing information about biological materials. They offer simple sample preparation, the ability to non-invasively image samples in situ, the ability to simultaneously image several different properties, and compatibility with many other imaging techniques. The earliest applications of optical imaging to measure cellular membranes revealed their basic structure and their dynamic properties at the ensemble level. Many important molecular assemblies in biological membranes occur in the

nanometer scale, thus diffraction-limited optical techniques are unable to resolve them. The development of super-resolution optical imaging techniques has accelerated the study of biological membranes, sometimes one molecule at a time. Within the past few years, multimodal and multicolor imaging approaches were developed to facilitate multivariable imaging of membranes, primarily with fluorescence contrast. Recent advances in Raman scattering techniques have paved the path to obtain chemical information at the nanoscale level. The introduction of novel and highly selective probes, advanced light sources, novel detectors with fast detection rates and high quantum yields, modifications to optics that provide optimized signals as well as recent big data efforts have all helped improve image quality and analysis, and have thus lead to a better understanding of membrane-related phenomena.

This review summarizes the optical imaging instrumentation that has recently been developed or is being developed in order to measure membrane organization and dynamics as well as some of the key applications of these instruments for membrane studies. The developments and applications of fluorescence and Raman-based imaging methods are covered. Atomic force microscopy, mass spectroscopy, and electron microscopy methods are useful for revealing complementary details about membrane structure and dynamics, but will not be covered herein, nor will studies of model membranes, such as those using supported lipid bilayers.

2. Fluorescence Microscopy Techniques

Fluorescence techniques have been valuable tools for the study of biological membranes for many decades. They have the advantages of allowing live cell imaging with fast time resolution and the sensitivity to measure single fluorescent molecules or probes. Recent developments in sub-diffraction or super-resolution fluorescence-based techniques have expanded our knowledge of membrane structure and dynamics. In many cases, these super-resolution imaging techniques have been used in combination with well-established fluorescence techniques to reveal information about membrane nanostructure and dynamics that cannot be measured using a diffraction-limited analysis volume.

The well-established fluorescence imaging techniques that have been used for biological membrane studies include: fluorescence lifetime imaging (FLIM), fluorescence resonance energy transfer (FRET), fluorescence recovery after photobleaching (FRAP), single particle tracking (SPT), and fluorescence correlation spectroscopy (FCS). FLIM is widely used to measure protein-protein interactions, protein conformational changes, and lipid domains within plasma membranes.[2,3] The fluorescent probe's lifetime is used to generate the image, which has the benefit of being independent of probe concentration. FRET is also used to elucidate membrane protein interactions and conformational kinetics,[4-9] and is exquisitely sensitive to a separation distance of less than 10 nanometers. FRAP,[10-14] SPT[15,16] and FCS[17,18] are well suited to measure membrane dynamics. FRAP is an ensemble technique in which the target is linked to a fluorescent probe and a selected region is photobleached with a high-power laser beam. Fluorescence recovery over time at the bleached region is used to analyze the diffusion properties of the labeled target. In SPT, a membrane component is tagged with a photostable fluorescent probe (e.g., quantum dots) and the movement of the probe is recorded over time to generate the trajectory of the biomolecule. The statistical analysis of the trajectories can provide information about heterogeneous populations and rare populations that may be averaged out of the ensemble FRAP signal. FCS is based on the statistical analysis of the fluorescence intensity fluctuations of a small number of fluorescent probes. All factors that alter the fluorescence fluctuations such as dynamics, molecular kinetics and photophysical properties of the probes (dark and triplet states) can be measured using FCS.

Total internal reflection fluorescence microscopy (TIRFM) and light sheet microscopy (LSM) are two illumination geometries that have been widely used to image cell membranes and their components. These techniques image thin optical sheets of less than a couple hundred nanometers (TIRFM) and a couple of microns (LSM), and reject the extensive background from the bulk of the cell. This is important in order to image the six to ten-nm thick biological membrane with a high signal-to-background ratio. Recent applications of TIRFM include imaging membrane protein clusters,[19,20] the structure and dynamics of membrane transporters,[21-25] and lipid rafts.[26,27] LSM has been recently used to image the dynamics and organization of membrane proteins[28] as well as to study the changes of membrane dynamics in dividing cells.[29] Although these techniques provide signal selectivity in the axial direction (i.e., perpendicular to

the focal plane), in the lateral direction they are inherently diffraction limited, and by themselves are not well suited for measuring the nanoscale structure and dynamics of membranes.

2.1 Single Molecule Localization Microscopy (SMLM)

SMLM techniques such as photoactivated localization microscopy (PALM)[30,31] and stochastic optical reconstruction microscopy (STORM)[32,33] have gained widespread use for imaging biological membranes. PALM uses photoactivatable fluorescent proteins, and was first independently introduced by Betzig et al.[30] and Hess et al.[31] (wherein it was termed fluorescence photoactivation localization microscopy, FPALM). STORM uses organic molecules as SMLM probes and was first introduced by the Zhuang group.[32]

The SMLM techniques rely on the sequential activation of sparse subsets of fluorescent probes and the time-resolved localization of these probes with nanometer precision. An order of magnitude better spatial resolution can be achieved with SMLM technique compared to diffraction-limited optical imaging techniques. Typical SMLM instrumentation consists of an epi-fluorescence microscope, lasers for activation and excitation of the fluorophores, and an array detector with high sensitivity and fast acquisition rates. The lasers are focused at the back focal plane of a high-numerical-aperture oil-immersion microscope objective to produce a broad (global) illumination profile at the sample plane. The very low read noise of electron-multiplying charge-coupled device (EMCCD) cameras or scientific complementary metal oxide semiconductor cameras allows for efficient signal collection from single molecules. The signal detected from a single emitting probe is fit to a Gaussian profile or similar function to localize emitter position with precision in the nanometer range. Controlling the on and off state switching of the probe is crucial to maintain a low number of emitters in each frame of the collected data. This is generally achieved with high-power lasers and using additives such as thiol, phosphates and oxygen scavengers in the imaging medium. For techniques that require the acquisition of images over time, as required for SMLM, drift correction is commonly required to extract accurate information from the images.

Photoactivatable, photoconvertible or reversibly photoconvertible fluorescent proteins have been used for PALM.[34] Light irradiation converts the photoactivatable probes from the

nonfluorescent form into the fluorescent form. Photoconvertible and reversibly photoconvertible probes are converted from one fluorescent state into another fluorescent state (i.e., emitting one color to another color). This cycle can be repeated many times in reversibly photoconvertible fluorescent proteins. These proteins are genetically encoded and are co-expressed with the target, which leads to specific labeling and a high expression density suitable for PALM. This super-resolution technique was able to image the spatial distribution of membrane proteins and lipid-enriched nanodomains in cell membranes.[35-42]

Dual color PALM has the ability to image the nanoscale co-association of two cell membrane components.[43-45] The downstream signaling molecules of T cell antigen receptor[44] and the effects of ethanol and naltrexone on the distribution of glycosylphosphatidylinositol and mu-opioid receptor[45] were studied using dual color PALM, where the sequential activation of two fluorescent proteins was achieved by altering the activation laser irradiance. Gabor et al. showed the colocalization of the cytokine receptor family members with Caveolin-1 protein using simultaneous activation of Dendra (λ_{ex}: 490 nm, λ_{em}: 507 nm before photoactivation and λ_{ex}: 553 nm, λ_{em}: 573 nm after photoactivation) and PAmCherry (λ_{ex}: 564 nm, λ_{em}: 595 nm) fluorescent proteins.[43] Signal from these proteins were simultaneously detected by separating the emission signal into two paths using appropriate dichroic mirrors and emission filters prior to directing the signal onto an EMCCD camera. Localized molecules were identified using a ratio of signal in the red channel divided by the intensity in both channels (0.55-0.64 for Dendra and 0.68-0.75 for PAmCherry).

PALM combined with single particle tracking (sptPALM) enables the study of heterogeneity in the dynamics of membrane components with high spatial and temporal resolution.[46,47] In contrast to traditional single particle tracking methods, sptPALM generates a higher density of single-molecule trajectories in the membrane of a single cell. The lateral dynamics and nanoscale organization of purinergic receptor P2X7 in neuronal membranes were imaged with sptPALM. Two receptor populations: a rapidly diffusing fraction and a clustered fraction (the clusters were ~100 nm diameter) were detected.[48] Two color sptPALM with spectrally resolved PATagRFP (λ_{ex}: 562 nm, λ_{em}: 595 nm) and PAGFP (λ_{ex}: 475 nm, λ_{em}: 517 nm) was used by Verkhusha and coauthors to image the dynamics of two transmembrane proteins in the plasma membrane of COS-7 cells.[49]

PALM is a versatile technique capable of imaging nanoscale features, but it does require transfected fluorescent proteins that are linked to the target, thus the study of endogenous membrane components is not possible. The linked fluorescent protein can be bulky and may also alter the dynamics of the targeted biomolecules depending on the cloning location.

STORM is based on switching organic fluorophores between the on and off fluorescent states to achieve the stochastic activation of a small subset of these molecules. The fluorophores are converted into a long-lived triplet state called a dark state using a high irradiance excitation laser and/or using additives in the imaging medium. In order to achieve accurate single molecule localization, only a small fraction of fluorophores can be activated at the same time, leading to one or fewer excited molecules within a diffraction-limited area. The distribution and clustering patterns of several receptor proteins were imaged in cell membranes using STORM.[50-58]

Similar to dual color PALM, dual color STORM can measure the nanoscale co-association of membrane components using two spectrally distinct fluorophores tagged to the membrane components. Sparse populations of both fluorophores are simultaneously activated and excited, and the emission from both fluorophores is directed onto the detector using a dual-channel image splitter with the appropriate filters (or multiple detectors).[59-63] Dual color STORM with Atto 565 and Atto 647N revealed the clustering of two different cell antigen receptors in spatially distinct areas in B cell membrane.[61]Activation of B cells reduced the cluster size for both receptors, and the activation of one receptor had a minimal affect on the clustering of other receptor.

A combination of PALM and STORM techniques has also been used to simultaneously image multiple components within the cell membrane.[64-73] “Ordered” and “disordered” lipid domains as well as the localization of clustered B cell receptor into ordered domains were measured in mouse B lymphoma cell membranes using this approach (Figure 1).[69] The combinations of fluorescent probes in this study were Atto 655 with Alexa Fluor 532 (i.e., dual color STORM) to localize ordered and disordered lipid domains, and Atto 655 with mEos3.2 fluorescent protein (i.e., PALM/STORM) to measure colocalization of B cell receptors into ordered domains. The latter probe pair required three lasers: 647-nm solid-state laser, 630-nm diode laser (excitation of mEos3.2), and a 405-nm diode laser (photoactivation of mEos3.2). Laser irradiances were adjusted between 5 to 20 kW/cm^2 to achieve favorable conditions for

single molecule/protein localization, and the emission was separated into two channels prior to reaching the detector.

Figure 1

A recent combined PALM/STORM study by Bernhem et al. measured the effect of protein overexpression on the cell membrane of HEK293a cells during transient transfection.[72] The endogenous and exogenous membrane protein distribution of Na,K-ATPase were quantified, and revealed there was a competition between endogenous and exogenous expression during the transient transfection state. The exogenous population was measured by PALM whereas the endogenous versus exogenous population was quantified with STORM. Forty one hours post transfection, the total plasma membrane concentration of Na,K-ATPase increased by 63% over the concentration measured prior to transfection; and the amount of Na,K-ATPase attributed to endogenous expression was only 16%. Alexa Fluor 647 was used for STORM imaging with a 405-nm activation laser and 642-nm excitation laser. PALM imaging was achieved with mMaple3 fluorescent protein using a 405-nm activation laser and 561-nm excitation laser.

In another study utilizing PALM/STORM, the organization of Nipah virus proteins on the plasma membrane was detected.[73] Nipah is a biosafety level 4 human-to-human transmitted virus. The results showed clusters of virus proteins, such as attachment glycoproteins and fusion glycoproteins, were randomly distributed on the mammalian PK13 cell membrane regardless of whether virus matrix proteins were present or absent. This contradicts the previously proposed models developed using electron microscopy and biochemical methods, which show matrix proteins assist in the arrangement of glycoproteins into assembly sites at the plasma membrane. The PALM and STORM data were acquired sequentially; GFP was used for PALM with 488 nm excitation and Alexa Fluor 647 and Cy3B were used for STORM with 639-nm and 532-nm excitation lasers, respectively. A 405-nm laser activated the probes. To facilitate photoswitching, oxygen scavenging buffers were used that contained 50 mM mercaptoethylamine or 140 mM β-mercaptoethanol.

The photophysical properties of the probes are critical to SMLM techniques. Assuming the noise is constant, the larger the number of detected photons, the better the localization

precision and the spatial resolution of the reconstructed image. Longer dark states help to maintain low duty cycles so that a small subset of probes can be activated and reduce multiple detection events for the same probe. Alexa Fluor, Atto, and cyanine dyes are commonly used as STORM probes. Photoactivatable organic probes, wherein a structural rearrangement occurs upon photoillumination at a specific wavelength to generate the on state, have also gained interest for SMLM imaging. Re-activation and photoswitching of these probes are negligible due to the irreversible nature of the photoactivation. The photoactivatable probes cage 500 and cage 552 were used as SMLM probes to image the oligo/dimerization of G protein-coupled receptors with approximately eight nm resolution.[74] A 390 nm laser was used for activation; 491 and 561 nm lasers were used to excite the activated cage 500 and cage 552, respectively. BODIPY-based photoactivatable compounds are also promissive SMLM probes for the study of membrane components.[75] These probes can be activated and excited using low power visible (~500 nm) light, and live cell imaging of membrane components is possible. Huang and coworkers introduced blinking carbon dots as SMLM probes due to their low duty cycle (~0.003), high photon count per switching event (~8000), and a high resistance to photobleaching, which is a common problem for small molecule SMLM probes (e.g., Alexa Fluor 647 and Cy5).[76] They used blinking carbon dots to image the distribution and the clustering of chemokine receptor CCR3 on the HeLa membrane.

Sharonov and Hochstrasser developed the technique called points accumulation for imaging in nanoscale topography (PAINT) as another approach to obtain the on and off switching required for SMLM probes.[77] The technique does not require a photoactivation step to generate the on state. In PAINT, fluorescent probes are freely diffusing in the imaging medium. The probes continuously and stochastically bind and unbind from the imaging target. When the probe immobilizes on the target, the signal is obtained, and then disappears when the probe dissociates from the target or photobleaches. Numerous probes can be used, and the binding rate is easily managed by controlling the probe concentration. Since the probes dynamically bind and unbind to the target over the course of the experiment, all of the target molecules have the potential to be imaged, even if the target density is high and simultaneous binding of the probe to all targets is prohibited. The first demonstration of PAINT took advantage of the photophysical properties of Nile Red, which is not fluorescent in aqueous solutions but is highly fluorescent in the hydrophobic membrane environment.

As first described, PAINT was limited to short analysis times and single molecules could not be tracked over long times. This problem was overcome with universal PAINT (uPAINT) developed by Giannone and Hosy, which enabled the real-time dynamic imaging of live cell membrane components.[78] This method involves the use of oblique illumination of the imaging target with diffusing fluorescent ligands in the solution. Long single-molecule trajectories are obtained with high densities that reveal the local diffusion properties of target components. Dual color uPAINT with two different fluorophores (one bound to the ligand epidermal growth factor and another bound to a specific antibody, panitumumab, that prevents ligand activation by blocking the binding site) was combined with FRET to study the nanoscale localization and ligand activated dimerization of epidermal growth factor receptor (Figure 2).[79] The authors found that the activated dimers were preferentially located at the edge of the cell, and note that they were able to image the receptor moments after ligand binding occurred (i.e., the event that generated the signal), which would not have been possible with SMLM techniques that require photoswitching.

DNA-PAINT takes the advantage of the reversible binding kinetics of DNA hybridization.[80,81] The docking DNA strand is bound to a primary or secondary antibody specific to the imaging target and the imager DNA strand is bound to a fluorescent probe. DNA-PAINT elucidated the distribution of single ryanodine receptors in cardiac myocytes.[82] The random and unconstrained arrangement of ryanodine receptors as well as the stoichiometry of the co-clusters of ryanodine receptor and the regulatory protein junctophilin-2 were quantified. In another study, the nonhomogeneous distribution of five types of receptor tyrosine kinases in the plasma membrane were identified with five different fluorescent probes bound to different DNA imager strands.[83]

Figure 2

SMLM techniques including PALM and STORM provide nanoscale resolution with simple instrumentation compared to many other super-resolution microscopies, but they require post-capture processing and image reconstruction. Other disadvantages include slow data

acquisition due to the large number of acquired frames for each reconstructed image, and the often required high irradiances are not ideal for many cellular studies. Simultaneous activation of multiple probes in a diffraction limited spot, insufficient or incomplete target labeling, limited probe accessibility due to high target packing density may all underestimate the quantity of target biomolecules. Overestimation of the probes is also possible and may result in imaging artificial clusters that do not exist in the membranes.[84] These artifacts are attributed to high photoswitching rates as well as high emitter densities. In multi-color studies, and particularly in PAINT studies, different affinities of the probes for their targets also affect the imaging quality of different targets. Therefore, the quantification of densely packed membrane components using SMLM techniques may not always be reliable.

2.2 Super-resolution optical fluctuation imaging (SOFI)

Super-resolution optical fluctuation imaging (SOFI)[85] developed by Dertinger et al. generates nearly background-free high-contrast super-resolution images with a short acquisition time of around a few seconds. This method also requires the stochastic switching of the probe between two different emission states, but uses higher-order statistical analysis to measure the intensity fluctuations over time. Contrary to STORM or PALM, SOFI can be used when multiple probes are simultaneously emitting within a diffraction-limited area.[86,87] High-resolution SOFI images are constructed by using spatio-temporal cross-cumulants.[88] The brightness, concentration, and emitting state lifetimes can be extracted by analyzing several cumulant orders of the same data set.[89] Balanced SOFI (bSOFI) was used to quantify the distribution of CD4 glycoprotein and mutant variants in the plasma membrane of Jurkat T cells (Figure 3).[90] bSOFI-based cluster analysis calculations do not depend on molecular localization coordinates, nor any of the user-defined parameters that are required for SMLM-based cluster analysis. Also, bSOFI is not subject to measuring artificial clusters that arise in SMLM images due to multiple blinking events from the same probe. Although this method allows for a biased-free analysis of cluster formation, membrane dynamics cannot be revealed due to the need to image fixed cells.

Zhang and coworkers introduced photochromic SOFI (pcSOFI), which enables nanoscale imaging of events in live cells using the advantage of strong intensity fluctuations generated by reversible photochromic probes.[91] As a proof of concept for imaging cell membrane components,

a protein that targets sphingolipid and cholesterol enriched microdomains (Lyn kinase protein) was tagged with Dronpa fluorescent protein and imaged using pcSOFI with ~120 nm resolution.[91] The same group recently introduced a new class of fluorescent biosensor for pcSOFI imaging called fluorescence fluctuation increase by contact (FLINC).[92] In these biosensors, the fluorescence fluctuation is controlled by the proximity of two fluorescent proteins. The resulting single molecule fluorescence fluctuations are recorded over time, then the pcSOFI values at subpixel resolution are calculated using pairwise cross-cumulants with suitable pixel pairings. Nanoscale activity maps are generated using the collected pcSOFI values. This technique was used to image protein kinase A activity in nanodomains in the plasma membrane of HeLa cells. Although the best reported resolution of SOFI techniques has not yet reached the levels achieved with PALM or STORM, fast image acquisition rates and the ability to use a wide range of fluorescent probes are advantages of SOFI techniques.

Figure 3

2.3 Stimulated Emission Depletion Microscopy (STED)

Similar to SMLM and SOFI techniques, STED is also a far-field super-resolution imaging technique that requires specific photophysical properties of the fluorescent probe.[93] STED was introduced by S. W. Hell in 1994. With reported lateral resolution levels better than ten nm,[94-96] STED is a promising tool to study membrane components. In a STED experiment, the lateral resolution is improved by reversibly depleting the signal from fluorophores around the periphery of the observation spot. This requires two laser wavelengths. The excitation beam is spatially overlapped and temporally offset with a red-shifted doughnut-shaped depletion beam to eliminate spontaneous fluorescence from molecules within the doughnut profile. Only molecules within the center of the excitation profile contribute to the spontaneous fluorescence signal. When the laser beams are scanned over the sample (or vice versa), a sub-diffraction image is produced. The axial resolution can also be improved with at least three different approaches: using a bottle-shaped focused beam to axially confine the fluorescence,[97] combing STED with 4Pi microscopy,[98] or combining STED with selective plane illumination microscopy.[99] The principles of STED microscopy and its biological applications have been broadly discussed.[100-102] The earliest applications of STED for imaging biological membranes

include studies of membrane protein clusters, lipid nanodomains and their interactions.[103-108] In a recent study, the spatial colocalization within the membrane of mortalin, a mitochondrial chaperon protein that is overexpressed in cancer, with the complement membrane attack complex C5b-9 was imaged with 35-nm spatial resolution using two color STED.[109] The specific labeling of the target was achieved using antibodies, and the fluorescent probes were ATTO 594 and Abberior Star 635p. Both represent common classes of fluorophores used in STED imaging. As is common for many scanning imaging techniques, fixed cells (human leukemia cells) were studied. Two excitation beams of 590 nm and 640 nm were used to simultaneously image the signal from ATTO 594 and Abberior Star 635p, respectively. A single depletion laser beam of 775 nm was suitable for both probes. Two acousto-optic modulators switched the excitation lasers sequentially, resulting in a quasi-simultaneous signal acquisition of two channels at the single pixel level. The resulting signal was spectrally resolved using dichroic mirrors and optical filters, and was directed to two single photon counting devices. The Image J program "Linear unmixing" was used to remove the spectral cross-talk between the two detection channels.

STED was used by Shin et al. to image the fusion pore behaviors in live cell membranes.[110] Single-color, two-color and three-color STED imaging was achieved using a tunable white-light excitation laser and hybrid detectors. A 592-nm or 660-nm depletion beam was used depending on the probe. Scanning in both the lateral and axial directions generated STED images with ~60 nm lateral resolution and ~150-200 nm axial resolution.

Lang and coworkers used STED microscopy to determine the packing density of the Alzheimer's disease-related amyloid precursor protein on fixed neuron-like human cell membranes.[111] Amyloid precursor protein and membranes were labeled with antibody-coupled Alexa Fluor 594 and Fast-DiO, respectively. They found that most amyloid precursor proteins that are associated with the plasma membrane are organized into structures containing 20 to 30 molecules confined within a region of 65 to 85 nm diameter. Nine amyloid precursor proteins were measured per micron squared. The same group studied syntaxin 1A protein clustering on human liver cancer cell (HepG2) membranes using continuous wave and pulsed STED techniques (Figure 4).[112] Their goal was to determine if it was possible to dissect independent mechanisms for membrane protein clustering. They

identified a hierarchy in membrane protein clustering, where "loose" clustering is due to the forces acting on the transmembrane segment and "tight" clustering is due to cytoplasmic interactions. They also reported that the size of the protein cluster does not necessarily scale with the number of proteins it contains.

Figure 4

The combination of STED with fluorescence correlation spectroscopy (STED FCS) can analyze a wide range of dynamic processes related to membranes with improved spatial resolution (Figure 4). Typically, the analyzed area in a FCS experiment is diffraction limited. In STED FCS, the fluctuations in fluorescence intensity are detected and statistically analyzed to study the diffusion properties or binding interactions of the fluorescent species within a sub-diffraction volume. The analyzed area is reduced to a few or tens of nanometers. This allows nanoscale heterogeneities to be measured that would otherwise be averaged out of a confocal analysis volume. Lipid dynamics have been measured in model membranes using STED FCS[113] and gated STED FCS wherein the detected signal is time-gated to optimize the spatial resolution.[114] Time-correlated-single-photon-counting photon filtering removes the background that is produced from incomplete depletion within the doughnut profile and enhances the spatial resolution. The molecular organization and the diffusion properties of fluorescent lipid analogs and glycophosphatidylinositol-anchored proteins in live PtK2 or CHO cell membranes and cell-derived giant plasma membrane vesicles (GPMVs) were analyzed using STED FCS.[115]

STED has also been coupled with scanning FCS (sSTED FCS) by Bizzarri and coworkers.[116] In this combination technique, the signal was rapidly recorded along a line or a circle. Heterogeneity in lipid and protein diffusion was mapped with sSTED FCS in live cell membranes with 60-nm spatial resolution and submillisecond temporal resolution. This method has advantages over single-point STED FCS because molecular trajectories can be simultaneously detected at different positions on the membrane, and heterogeneous behaviors can be measured with nanoscale resolution. Moreover, single point FCS measurements require precise knowledge of the analysis volume to obtain accurate diffusion properties, whereas scanning FCS overcomes this requirement. Fluorophore photobleaching and background are also problematic in single point STED FCS experiments, but the lower dwell times of scanning FCS

reduce the photobleaching that may lead to false diffusion properties.[117] A disadvantage of sSTED FCS also comes from the lower dwell times per pixel, which leads to decreased signal-to-noise ratios in the correlation curve. The method, however, was shown by Eggeling and coworkers to be suitable to measure the diffusion dynamics of fluorescently labeled phospholipids, cholesterol and sphingolipids in PtK2 cell membranes.[118] The spatiotemporal mapping of Atto647N-labeled phosphatidylethanolamine and sphingomyelin in PtK2 cell membranes as well as the quantification of cholesterol dynamics in different cell lines as a function of growth time were also measured using sSTED FCS.[119] Additionally, the dynamics of Atto647N-labeled sphingomyelin and phosphatidylethanolamine in Cos-7 cell membranes were mapped.[117] The authors report there was a lot of heterogeneity in the signal measured between and within cells, which was not captured by other STED FCS techniques, and that the inversely correlated diffusion coefficient and local dye concentration were an indicator that the lipid species become temporally trapped, for example, by the glass substrate on which the cells were spread or an unknown cellular component.

In contrast to SMLM techniques that requires a series of images to be collected over time, fast data acquisition rates have been reported with STED. In a STED experiment, neither post-image processing nor special imaging buffers are required. While the high laser irradiances generally limit the choice of fluorophore down to a few classes of the most photostable fluorophores, there is a wide selection of excitation wavelengths available for STED. Live cell membrane imaging is possible using lower irradiances, generally at the expense of spatial resolution. Continuous wave STED enables fast imaging and is thus suitable for live cells, but the achievable resolution is limited compared to pulsed STED when using the same irradiance. Overall, the STED instrumentation is more complicated than most SMLM setups.

2.4 Super-resolution Structured Illumination Microscopy (SR-SIM)

SR-SIM is a wide-field imaging technique that uses a structured pattern of the illumination light to excite the florophores in the sample. An overlay of two grids with different mesh sizes or at various angles generates moirè fringes that reveal sub-diffraction spatial information. Using non-linear responses, resolution lower than 100 nm is achieved. The sample preparation methods used with standard imaging techniques are compatible with SR-SIM, and any fluorophore with

reasonable resistivity to photobleaching is suitable. SR-SIM is also suitable for live cell imaging due to its use of relatively low excitation irradiances and fast imaging capabilities. Multicolor imaging of up to four colors has been reported.[120] Several studies have reported the use of SR-SIM to evaluate the relationship between the plasma membrane organization and cytoskeleton components.[121-125]

Figure 5

SR-SIM was also combined with other super-resolution imaging techniques such as SMLM to study biological membranes. STORM imaging results in a better spatial resolution than SIM, but SIM avoids the clustering artifacts in STORM images. SIM combined with STORM imaged the distribution of T-cell receptors in lymph nodes (Figure 5)[126] and acetylcholine receptors in postsynaptic membranes.[127] In the latter study, Alexa Fluor 647 was used to label the acetylcholine receptors and 3D-SIM was used to identify their stripe-like distribution pattern at the neuromuscular junctions. The enhanced resolution of STORM imaging revealed the receptor localization around the openings of junction folds (invaginations of the postsynaptic muscle membrane). In another study, a combination of SMLM and SIM revealed the correlation of the flows of plasma membrane and cortical actin in live T-cell synapses.[121] The nanoscale actin distribution was imaged in fixed cells using SMLM. Dual-color live-cell SIM images using a spatial light modulator to produce the structured illumination pattern were collected in TIRF mode. The SIM image series was analyzed using spatio-temporal image correlation spectroscopy, which measures the diffusion properties as well as the velocity vectors (magnitude and direction) of the imaging target.

Instant structured illumination microscopy (iSIM) improves the spatial resolution compared to diffraction-limited imaging without affecting the temporal resolution, and enable dynamic events to be imaged in live cells with higher acquisition speeds.[128] Information from excitation and emission point spread functions are optically combined to sharpen the image instantly. TIRF combined with iSIM was used to image plasma membrane components in U2OS cells with ~115 nm lateral resolution and with frame rates up to 100 Hz.[129]

SR-SIM techniques are superior to SMLM or STED techniques for live cell imaging when low light irradiances and fast imaging speeds are required. This technique, however, has not yet reached the spatial resolution that can be achieved with SMLM or STED techniques. Ongoing advances such as fast detectors, superior adaptive optics and advanced image reconstruction algorithms, are expected to improve the resolution to a level that is suitable for imaging many dynamic membrane events on the nanoscale.

2.5 Fluorescent Probes for Membrane Studies

The photophysical properties of probes play a major role in the quality of a fluorescence image. Genetically-encoded fluorescent protein labels are widely used, although the fluorescent protein may affect the natural function and/or dynamics of the biomolecule. The resulting data may not represent the properties of the endogenous pool of biomolecules. Immunolabeling with fluorescently-labeled antibodies targets specific membrane components, such as receptors, but this requires an available antibody to the target. Epitope tags (e.g., His, HA, FLAG, c-Myc) with the antibody corresponding to the tag are useful to label a specific target. They do not require a specific antibody for each membrane component, but genetically encoded epitope tags also eliminate the possibility of studying endogenous components. Nile red, Laurdan, DiI, DiD, DiO and fluorescent lipid analogs are widely used lipid mimetic probes for imaging membrane lipids. While these conventional probes are generally useful for imaging biological membranes, new minimally-invasive membrane probes with targeting specificity are needed. In addition to the specific photophysical properties required for each super-resolution imaging technique, membrane targeting probes should have solubility in imaging buffers, photostability to assure imaging for long analysis times without signal loss, low toxicity, and biocompatibility. A range of emission wavelengths is also desirable for multicolor imaging.

Several novel probes were recently introduced to image the lipid fraction of biological membranes. A permeabilization-tolerant membrane imaging probe was developed by linking three species: cholesterol-polyethylene glycol, fluorescein isothiocyanate, and amine-rich glycol chitosan.[130] This probe was used to simultaneously image cell membranes with intracellular

components in fixed cells. N-[[40-N,N-diethylamino-3-hydroxy-6-flavonyl]-methyl]-N-methyl-N-(3-sulfopropyl)-1-dodecanaminium was synthesized as an environment sensitive probe.[131] This probe had dual emission peaks based on the lipid order in its surrounding environment, thus it can be used as a ratiometric probe for imaging the ordered and disordered lipid domains in membranes. In another study, a two-photon activatable red emitting styrylpyridine-based small molecule rotor was developed.[24] The membrane affinity of this probe is due to the amphipathic nature of the molecule. The high membrane viscosity limits free molecular rotation and results in enhanced fluorescence.

Another newly developed membrane probe consisting of three linked components: cholesterol, phospho-D-thyrosine and 4-nitro-2,1,3-benzoxadiazole fluorophore was used to image the real time dynamics of cell membranes.[132] GPI-anchored enzymes in lipid rafts activate the probe by cleaving the phosphate group, and the activated probes self-assemble on the plasma membrane. A membrane-targeting two-photon-excitable nitric-oxide probe was developed by attaching a quaternary ammonium compound and a long alkyl chain into 4-amino-1,8-naphthalimide.[133] This bipolar structure is specifically localized in the plasma membrane. Initially it has a negligible fluorescence, but upon binding with nitric oxide its fluorescence is enhanced. In another study, a conformationally induced off-on probe was developed by linking hexamethylenediamine with sunitinib and pyrene to target and image the tyrosine kinase receptor protein in cell membranes.[134] The TLSHalo probe was developed to image the potassium ion transportation in cell membranes.[135] This probe specifically targets Halo-tag expressing proteins on the cell membrane and is fluorescent upon binding with potassium; the reported selectivity over sodium is high.

Fluorescent conjugated-polymer nanoparticles have advantages as imaging probes due to their high quantum yield, photostability, biocompatibility, and ease of surface modification. Although for some applications, their larger size may alter the membrane properties. Conjugated polymer nanoparticles with poly(fluorene-co-phenylene) linked to the drug plerixafor were used to target CXCR4, a G protein-coupled receptor in the cell membrane.[136] The blue-emitting nanoparticles showed good water solubility, selective membrane targeting, and a low toxicity that is suitable for live cell membrane imaging. Red-emitting conjugated-polymer nanoparticles with two photon absorptivity were also developed as membrane probes.[137] The membrane

selectivity is due to the hydrophobic interactions of the polymer's aliphatic chains with membrane lipids. A cationic polythiophene derivative: poly((3-((4-methylthiophen-3-yl)oxy)propyl)triphenylphosphonium chloride) was introduced as an imaging agent for adenosine triphosphate in cell membranes.[138] Qian and coworkers developed lectin-functionalized lanthanide-doped upconversion nanoparticles to image the glycan molecules within the cell membrane.[139] They used this probe to identify cancer cells by imaging the glycan distribution pattern in cell membrane. Gold nanoparticles bioconjugated with rationally designed peptides were developed for integrin selective imaging on cell membrane.[140] This probe is excitable with two photons and enables quantification of integrins due to the enzymatic catalysis of the probe at the integrin site. Semiconductor quantum dots labeled with phenylboronic acid were developed as imaging probes to detect sialic acids in membranes.[141] This probe enabled the imaging of sialylated glycoproteins in live PC12 cell membranes. These novel probes that report on a specific endogenous membrane component or membrane function are promising for future use with super-resolution imaging techniques.

3. Raman Imaging

Raman imaging is a chemically-specific label-free technique that allows the simultaneous imaging of multiple membrane components. The fundamental details of Raman scattering as well as the previous applications of Raman techniques for biomaterial analysis,[142] including membranes and lipid-rich organelles has been previously discussed.[143] The low cross section of spontaneous Raman scattering, and the resulting weak signals, generally mean that signal enhancement techniques are required in order to image membrane components at relevant cellular concentrations. Surface-enhanced Raman spectroscopy (SERS) and tip-enhanced Raman spectroscopy (TERS) have been used to image cell membranes.

3.1 Surface-Enhanced Raman Spectroscopy (SERS)

In SERS, the Raman scattering is greatly enhanced for molecules in close contact with a nanostructured plasmon substrate consisting of metals such as gold, silver, or copper. Since the membrane is the only organelle in close proximity when cells are spread on a SERS substrate,

membrane selectivity can be achieved. SERS spectra of lipids, amino acids and carbohydrates in live red blood cell membranes were recorded using nano-clustered silver as the plasmonic substrate (Figure 6).[144] Raman peaks corresponding to membrane components could not be identified by spontaneous Raman spectroscopy due to the large signal from bulk hemoglobin within the cell. In another study, Fogarty et al. suggest their spectral mapping of the endothelial plasma membrane using SERS with silver-intensified gold (metallic silver shell around the gold nanoparticle) as the plasmonic substrate showed evidence of a heterogeneous distribution of membrane components.[145] The positively-charged gold plasmonic nanoparticles were linked with the net negatively charged glycocalyx (the glycoprotein and glycolipid enriched covering around the endothelial cell membrane) and were evenly distributed across the glycocalyx. A 100-fold signal enhancement of the spectral signal from the membrane was observed.

Figure 6

In order to image a specific membrane component with SERS, a targeting label must be added to the SERS substrate. Lipid raft membrane domains were imaged by incorporating a ring-opened alkyne steroid-analogue probe into the cell membrane.[146] This analogue formed microdomains that resemble the lipid rafts in membranes. Alkyne tags are commonly used because they have a unique Raman peak at ~2120 cm^{-1} and enable the imaging of biomolecules over long times with minimal effects on their intrinsic properties. Alkyne tags have also been used to image membrane proteins such as folate receptors and luteinizing hormone-releasing hormone receptors in HeLa cells.[147,148] In these HeLa cell studies, 4-ethynylbenzenethiol derivatives were modified with various substituents to introduce the ability for multiplexed imaging. These alkyne reporters were encapsulated into polyallylamine-containing Au-Ag nanoparticles with a thiol-gold bond. By incorporating the appropriate ligand, specific receptors were imaged.

In a recent study, wide-field Raman imaging was combined with SERS for bioimaging of phosphatidyl serine in human colon (LoVo) cell membranes.[149] The spatial resolution of wide-field Raman imaging was improved to 100 nm using standing-wave total-internal-reflection microscopy (SW-TIRM) with narrow band-pass filters. Similar to the SIM technique discussed above, the spatial resolution is enhanced by using spatially patterned light to illuminate the sample in total internal reflection mode to reduce the illumination depth, which enhanced the

signal-to-background ratio. A metal core coated with 4-mercaptobenzoic acid and embedded in a poly(vinylpyrrolidone) shell was used as the SERS substrate and phosphatidyl serine was imaged with antibody-coated SERS nanoparticles.

SERS enables imaging with enhanced signals compared to spontaneous Raman scattering, but the routine sensitivity is still not as good as what can be commonly achieved with fluorescence. Single molecule SERS experiments with biological membranes remain a challenge, and as a result, SERS measurements provide an average signal of many biomolecules. In addition, all molecules can potentially contribute to the Raman signal, so as mentioned previously, selective measurements often do require a label. Reproducible SERS signals also remain a challenge to be solved. While many SERS measurements use low laser irradiances, photodamage of the SERS substrate or sample is still possible with prolonged acquisition times.[150-152]

3.2 Tip-Enhanced Raman Spectroscopy (TERS)

Tip-enhanced Raman spectroscopy (TERS) combines the chemical sensitivity of SERS and the nanoscale spatial resolution of scanning probe microscopies, and permits molecular level imaging of membranes. Scanning probe techniques such as scanning tunneling microscopy, atomic force microscopy, sheer force microscopy, and scanning near-field optical microscopy have been used in TERS. The concept of TERS was introduced by Wessel in 1985.[153] In 2000, four groups independently reported TERS results that proved the applicability of the technique.[154-157] TERS uses focused laser illumination on a metal or metal-coated tip, which creates a localized, strongly-enhanced electromagnetic field at the tip apex. While scanning the tip in close proximity to the sample (a separation distance equal to roughly the wavelength of light), enhanced Raman scattering is measured from molecules close to the tip. Spatial resolution in the tens of nanometer range or less is achieved. Multiple studies reported subnanometer spatial resolution with TERS.[158-160] The fundamentals of the technique and recent advances beyond the measurement of cell membranes are discussed in several reviews.[161-165] The earliest applications of TERS for membrane studies include imaging model cell membranes (i.e., lipid bilayers),[166-169] bacterial[170,171] and viral surfaces.[172-174]

In a recent study using TERS, Gram positive and negative bacterial species were differentiated based on the Raman signal of their membranes.[175] Gold nanoparticles with a 100

nm diameter were used at the apex of the TERS tip, and Raman data were collected with an upright microscope. The outer membrane of Gram negative bacteria consists of a lipid bilayer whereas the outer layer of Gram positive bacteria consists of a peptidoglycan cell wall. When the TERS tip was in contact with the Gram negative cell surface, the Raman signal was enhanced compared to the signal when the tip was out of contact. There was no difference in the 'tip in' and 'tip out' signals on Gram positive bacterial surfaces. Based on these spectral differences Gram negative and positive bacterial-types were distinguished.

Deckert and coworkers used TERS with silver-coated AFM tips to image plasma membrane components in human dermal-derived keratinocyte cells[167] and human colon cancer cells.[176] In the latter study, fixed cells were imaged with five second acquisitions to collect TERS data from up to a 270 × 162 nm area. Data collection was combined with multivariate data analysis (similar to vertex component analysis) to measure nanometer-sized lipid-and-protein-enriched domains in cell membranes. Lipid-enriched domains were measured primarily using phosphate bands and ranged from 10 × 40 nm to 20 × 20 nm in size; whereas protein enriched domains were measured using amide bands and were 10 × 30 nm to 30 × 70 nm in size. The exact protein composition within the domains could not be measured.

Schultz and coworkers imaged antibody-conjugated nanoparticles bound to fixed cell membranes using TERS.[177] A gold nanoparticle was also immobilized on the AFM tip and top illumination was used for TERS. In another study, the same group used ligand functionalized nanoparticles to chemically characterize $\alpha_v\beta_3$ integrins in the intact cell membrane of fixed human colon cancer cells using TERS.[178] The plasmonic interaction between the functionalized gold nanoparticle and the TERS tip selectively enhanced the amino acid signals from the nanoparticle-bound receptors on the membrane. Using the same technique, two integrin types on human colon cell membranes were identified and differentiated based on the spectral differences that result from slightly different ligand binding sites on these receptors (Figure 7).[179]

Figure 7

TERS is a valuable technique for measuring the nanoscale structure of the cell membrane, but membranes are highly dynamic, and TERS studies have been limited to imaging fixed cells. Live-cell imaging may also be problematic due to the need for imaging buffers. Emerging applications of TERS using a liquid medium[180-182] and improvements in the data

acquisition speed by Van Duyne et al.[183] will make this technique a promising tool for imaging structural and dynamic events in live cell membranes.

3.3 Raman-based techniques being developed for membrane studies

There are Raman techniques that are still in their infancy, but have promise for providing both the chemical information inherent in Raman scattering with the spatial resolution of super-resolution fluorescence imaging. While SERS and TERS require the use of plasmonic materials in close contact with the sample, the emerging Raman techniques do not have this requirement. Therefore the sample preparation is easier, and the potential of altering the membrane structure and dynamics during the imaging process is limited.

3.3.1 Sub-diffraction Femtosecond Stimulated Raman Spectroscopy

Frontiera and coworkers combined the concept of STED with femtosecond stimulated Raman spectroscopy (FSRS) to achieve sub-diffraction Raman imaging.[184] In this method, vibrational coherences in all Raman active modes are generated by overlapping two Gaussian-shaped picosecond and femtosecond beams. A doughnut-shaped decoherence pulse interferes with the FSRS signal and selectively eliminates the signal at the edge of the focal spot. The FSRS signal is generated only in the center where the decoherence beam has no intensity, which produces sub-diffraction images. Bacteriorhodopsin proteins in purple membrane sheets isolated from *Halobacterium salinarum* were imaged as a proof-of-concept for imaging biological membranes. Ongoing advancements to this technique are promising, particularly those that allow the use of reduced laser irradiances and further improvements to the spatial resolution.

Figure 8

3.3.2 Total Internal Reflection (TIR) Raman spectroscopy

As with TIRF imaging, TIR Raman imaging provides signal from molecules within a couple hundred nanometers away from a substrate, and can be used to provide enhanced signals from membrane components with a reduced contribution from the bulk of the cell. TIR Raman spectroscopy was first

demonstrated by Ikeshoji and coworkers in 1973[185] using a carbon disulfide sample on a glass substrate. Under TIR, an evanescent wave with a decaying electric field is produced near the substrate. One to two orders of magnitude enhancement in the Raman signal may result from the enhanced electric field produced under TIR. Monolayer sensitivity has been achieved using various TIR Raman formats (Figure 9).[186-189] While the TIR enhancement is typically less than the SERS enhancement, the TIR Raman signal is very reproducible, well modeled and does not require a roughened metal substrate. Also, the TIR Raman signal is collected over a longer distance than is possible with SERS, so the entire membrane and associated cytoskeleton can be probed. In addition, by varying the incident angle of light, the distance over which the Raman signal is collected can be varied; and tens of nanometer axial resolution is possible.[190,191] To demonstrate the compatibility of this technique with biological samples, a thin layer of bovine serum was imaged with a high signal-to-noise ratio.[192] As a proof-of-concept for membrane studies, a model planar supported lipid layer was imaged with the TIR Raman technique.[193] In contrast to epi-illumination, the Raman signal of cells collected with TIR illumination is expected to reduce signals arising from cytosolic and nuclear compounds, thus the plasma membrane could be imaged with a high signal-to-background ratio. While these developing Raman techniques are still in their infancy in regard to membranes studies, they are promising tools for future membrane studies.

Figure 9

4. Summary and Outlook

Biological membranes are highly heterogeneous and exhibit specific structural and dynamic properties that guide numerous cellular functions. Remarkable advances in optical techniques have enabled imaging with nanoscale spatial and fast temporal resolution, which are advantageous for membrane studies. This review reports the advances in fluorescence and Raman-based nanoscale imaging techniques and their recent applications to study the organization and dynamics of biological membranes. Localization-based super-resolution techniques including PALM and STORM enable high spatial resolution generally at the cost of temporal resolution. In contrast, STED and SIM generally offer faster acquisition rates with lower spatial resolution. Raman imaging techniques reveal spatially-resolved chemical

information, although they have not yet reached the superior performance for membrane studies that has been demonstrated for fluorescence techniques.

Even with many recent advancements, membrane imaging has not yet been optimized to solve some of the most crucial questions related to membrane biology. These complex questions may not be addressed with a single imaging (or analytical) technique, and future developments in multimodal instrumentation are promising. For instance, whole cell studies using combinations of SMLM with SIM, SPT and FRET, STED combined with SIM, FCS and FLIM as well as optical imaging methods combined with non-optical imaging techniques, such as atomic force microscopy, electron microscopy and mass spectroscopy, will enable information to be measured over multiple length, temporal, and chemical contrast scales. Of course, instrument developments, such as detectors with improved sensitivity, high quantum yields, larger pixel areas and faster response, will enhance the temporal resolution and facilitate the capturing of fast membrane dynamics. Advances in analysis techniques will facilitate the fast and improved data processing and image generation and may eliminate the co-localization and clustering artifacts generated during the data processing, particularly in SMLM.

Improved sample preparation techniques and probes are also important for achieving the best imaging quality. The majority of the cell membrane components are sensitive to fixation procedures, thus they may not be detected accurately in fixed cells. Fluorescent probes with high quantum yields, small size, good selectivity and controllable photophysical properties also need continual development. Bright white-light lasers make it possible to provide a range of wavelengths for multicolor imaging, yet suitable spectrally resolved fluorophores, particularly those that report on a specific component or function, are not always available. Additional environmental sensitive fluorophores would be beneficial to image various membrane processes such as ion transportation, variances of pH and electric potential.

Raman-based imaging approaches are commonly performed in fixed cell membranes due to lengthy imaging times (i.e., resulting from long acquisition times or scanning), which limits the dynamic information that can be measured. For the Raman techniques that have the best-reported spatial resolution to date, developing sensitive, reproducible, and biocompatible plasmonic SERS substrates and advances in TERS tip fabrication have the potential to provide selective imaging of single membrane components. Extension of TERS for compatibility with

liquid medium would be highly advantageous for imaging membranes in live cells. Emerging Raman techniques may also be beneficial for non-invasively imaging biological membranes without the use of SERS substrates or TERS tips.

While the nature of the cell membrane may seem to not warrant the need for super-resolution 3D (three dimensional) imaging techniques, they will permit the imaging of membrane processes and related intercellular signaling pathways as well as membrane topology and curvature. Visualization of the formation of exosomes from the cell membrane and their regulation by specific proteins is also possible. 3D optical methods are also helpful to image the membrane interactions of adjacent cells, and interactions with extracellular materials, for example viral or bacterial pathogens.

Author Information

Corresponding Author

*E-mail: esmith1@iastate.edu

ORCID ID

Chamari S. Wijesooriya: 0000-0001-5220-6519

Charles K. A. Nyamekye: 0000-0002-5190-3213

Emily A. Smith: 0000-0001-7438-7808

Notes

The authors declare no competing financial interest.

Author Biographies

Chamari S. Wijesooriya is a chemistry Ph.D candidate in the research group of Professor Emily A. Smith at Iowa State University. She received her B.S. degree in Chemistry at University of

Kelaniya, Sri Lanka and M.S. degree in Chemistry at Sam Houston State University. Her current research focuses on developing fluorescence methods for imaging membrane protein dynamics.

Charles K. A. Nyamekye is a chemistry Ph.D candidate in the research group of Professor Emily A. Smith. Prior to joining the Ames community in 2014, Charles received his B.S. degree in Chemistry with a minor degree in Mathematics at Framingham State University, Massachusetts. His work currently involves developing Raman scattering techniques to characterize biological materials and thin films, as well as, the development of a handheld biosensor to detect toxins in drinking water.

Emily A. Smith received her Bachelor's degree from Northwestern University and graduate degrees in chemistry from The Pennsylvania State University (M.S.) and University of Wisconsin-Madison (Ph.D.). Her postdoctoral appointment was at the University of Delaware and she was a Ruth L. Kirschstein National Research Service Award Postdoctoral Fellow at the Arizona Cancer Center, University of Arizona. She is currently Professor of Chemistry at Iowa State University and a Faculty Scientist at U.S. Department of Energy, Ames Laboratory. Her research focuses are instrument development for analysis of nanomaterials, plant and animal tissue; and understanding the molecular events that lead to organization of the cell membrane.

Acknowledgements

This work is supported by funding from NSF grant CHE-1709099. The authors thank Qiaochu Zhu and Sadie Burkhow for useful discussion and assistance in preparing this manuscript.

References

(1) Singer, S. J.; Nicolson, G. L. *Science* **1972**, *175*, 720-731.

(2)Becker, W. *Journal of Microscopy* **2012**, *247*, 119-136.

(3) Berezin, M. Y.; Achilefu, S. *Chemical Reviews* **2010**, *110*, 2641-2684.
(4) Gagnon, E.; Connolly, A.; Dobbins, J.; Wucherpfennig, K. W. In *The Immune Synapse: Methods and Protocols*, Baldari, C. T.; Dustin, M. L., Eds.; Springer New York: New York, NY, 2017, pp 259-289.
(5) King, C.; Wirth, D.; Workman, S.; Hristova, K. *Biochimica et Biophysica Acta (BBA) - Biomembranes* **2018**, *1860*, 2118-2125.
(6) Lam, J. G. T.; Vadia, S.; Pathak-Sharma, S.; McLaughlin, E.; Zhang, X.; Swanson, J.; Seveau, S.; Bement, W. *Molecular Biology of the Cell* **2018**, *29*, 270-284.
(7) Liu, Y.; Chen, L.-Y.; Zeng, H.; Ward, R.; Wu, N.; Ma, L.; Mu, X.; Li, Q.-L.; Yang, Y.; An, S.; Guo, X.-X.; Hao, Q.; Xu, T.-R. *The International Journal of Biochemistry & Cell Biology* **2018**, *99*, 114-124.
(8) Ma, Y.; Yamamoto, Y.; Nicovich, P. R.; Goyette, J.; Rossy, J.; Gooding, J. J.; Gaus, K. *Nature Biotechnology* **2017**, *35*, 363-370.
(9) Schihada, H.; Vandenabeele, S.; Zabel, U.; Frank, M.; Lohse, M. J.; Maiellaro, I. *Communications Biology* **2018**, *1*, 105, 1-8.
(10) Khandelwal, N. K.; Sarkar, P.; Gaur, N. A.; Chattopadhyay, A.; Prasad, R. *Biochimica et Biophysica Acta (BBA) - Biomembranes* **2018**, *1860*, 2308-2319.
(11) Kingsley, J. L.; Bibeau, J. P.; Mousavi, S. I.; Unsal, C.; Chen, Z.; Huang, X.; Vidali, L.; Tüzel, E. *Biophysical Journal* **2018**, *114*, 1153-1164.
(12) Lorén, N.; Hagman, J.; Jonasson, J. K.; Deschout, H.; Bernin, D.; Cella-Zanacchi, F.; Diaspro, A.; McNally, J. G.; Ameloot, M.; Smisdom, N.; Nydén, M.; Hermansson, A.-M.; Rudemo, M.; Braeckmans, K. *Quarterly Reviews of Biophysics* **2015**, *48*, 323-387.
(13) Ono, J.; Fushimi, S.; Suzuki, S.; Ameno, K.; Kinoshita, H.; Shirakami, G.; Kabayama, K. *FEBS Open Bio* **2018**, *8*, 1127-1134.
(14) Zhang, M.; Zhang, Z.; He, K.; Wu, J.; Li, N.; Zhao, R.; Yuan, J.; Xiao, H.; Zhang, Y.; Fang, X. *Analytical Chemistry* **2018**, *90*, 4282-4287.
(15) Carlo, M.; Maria, F. G.-P. *Reports on Progress in Physics* **2015**, *78*, 124601, 1-29.
(16) Shen, H.; Tauzin, L. J.; Baiyasi, R.; Wang, W.; Moringo, N.; Shuang, B.; Landes, C. F. *Chemical Reviews* **2017**, *117*, 7331-7376.
(17) Krieger, J. W.; Singh, A. P.; Bag, N.; Garbe, C. S.; Saunders, T. E.; Langowski, J.; Wohland, T. *Nature Protocols* **2015**, *10*, 1948-1974.

(18) Macháň, R.; Wohland, T. *FEBS Letters* **2014**, *588*, 3571-3584.
(19) Lucarelli, S.; Delos Santos, R. C.; Antonescu, C. N. *Methods Mol Biol* **2017**, *1652*, 191-225.
(20) Greitzer-Antes, D.; Xie, L.; Qin, T.; Xie, H.; Zhu, D.; Dolai, S.; Liang, T.; Kang, F.; Hardy, A. B.; He, Y.; Kang, Y.; Gaisano, H. Y. *J Biol Chem* **2018**, *293*, 6893-6904.
(21) Goudsmits, J. M. H.; van Oijen, A. M.; Slotboom, D. J. *Methods Enzymol* **2017**, *594*, 101-121.
(22) Tanaka, H.; Fujii, S.; Hirano, T. *Nat Protoc* **2014**, *9*, 76-89.
(23) Kisler, K.; Dominguez, R. *Methods Mol Biol* **2016**, *1366*, 175-187.
(24) Guo, L.; Zhang, R.; Sun, Y.; Tian, M.; Zhang, G.; Feng, R.; Li, X.; Yu, X.; He, X. *Analyst* **2016**, *141*, 3228-3232.
(25) Thal, L. B.; Tomlinson, I. D.; Quinlan, M. A.; Kovtun, O.; Blakely, R. D.; Rosenthal, S. J. *ACS Chem Neurosci* **2018**, DOI: 10.1021/acschemneuro.8b00350.
(26) Hirama, T.; Das, R.; Yang, Y.; Ferguson, C.; Won, A.; Yip, C. M.; Kay, J. G.; Grinstein, S.; Parton, R. G.; Fairn, G. D. *J Biol Chem* **2017**, *292*, 14292-14307.
(27) Yeow, I.; Howard, G.; Chadwick, J.; Mendoza-Topaz, C.; Hansen, C. G.; Nichols, B. J.; Shvets, E. *Curr Biol* **2017**, *27*, 2951-2962.
(28) Ponjavic, A.; McColl, J.; Carr, A. R.; Santos, A. M.; Kulenkampff, K.; Lippert, A.; Davis, S. J.; Klenerman, D.; Lee, S. F. *Biophys J* **2018**, *114*, 2200-2211.
(29) Aguet, F.; Upadhyayula, S.; Gaudin, R.; Chou, Y. Y.; Cocucci, E.; He, K.; Chen, B. C.; Mosaliganti, K.; Pasham, M.; Skillern, W.; Legant, W. R.; Liu, T. L.; Findlay, G.; Marino, E.; Danuser, G.; Megason, S.; Betzig, E.; Kirchhausen, T. *Mol Biol Cell* **2016**, *27*, 3418-3435.
(30) Betzig, E.; Patterson, G. H.; Sougrat, R.; Lindwasser, O. W.; Olenych, S.; Bonifacino, J. S.; Davidson, M. W.; Lippincott-Schwartz, J.; Hess, H. F. *Science* **2006**, *313*, 1642-1645.
(31) Hess, S. T.; Girirajan, T. P.; Mason, M. D. *Biophys J* **2006**, *91*, 4258-4272.
(32) Rust, M. J.; Bates, M.; Zhuang, X. *Nat Methods* **2006**, *3*, 793-795.
(33) Heilemann, M.; van de Linde, S.; Schüttpelz, M.; Kasper, R.; Seefeldt, B.; Mukherjee, A.; Tinnefeld, P.; Sauer, M. *Angewandte Chemie International Edition* **2008**, *47*, 6172-6176.
(34) Shcherbakova, D. M.; Sengupta, P.; Lippincott-Schwartz, J.; Verkhusha, V. V. *Annual Review of Biophysics* **2014**, *43*, 303-329.
(35) Mizuno, H.; Abe, M.; Dedecker, P.; Makino, A.; Rocha, S.; Ohno-Iwashita, Y.; Hofkens, J.; Kobayashi, T.; Miyawaki, A. *Chemical Science* **2011**, *2*, 1548-1553.

(36) Owen, D. M.; Williamson, D. J.; Magenau, A.; Gaus, K. *Nature Communications* **2012**, *3*, 1256, 1-8.
(37) Scarselli, M.; Annibale, P.; Radenovic, A. *Journal of Biological Chemistry* **2012**, *287*, 16768-16780.
(38) Sengupta, P.; Jovanovic-Talisman, T.; Skoko, D.; Renz, M.; Veatch, S. L.; Lippincott-Schwartz, J. *Nature Methods* **2011**, *8*, 969-975.
(39) Lillemeier, B. F.; Mörtelmaier, M. A.; Forstner, M. B.; Huppa, J. B.; Groves, J. T.; Davis, M. M. *Nature Immunology* **2009**, *11*, 90-96.
(40) Gabor, K. A.; Kim, D.; Kim, C. H.; Hess, S. T. *PLOS ONE* **2015**, *10*, e0117225.
(41) Hess, S. T.; Gould, T. J.; Gudheti, M. V.; Maas, S. A.; Mills, K. D.; Zimmerberg, J. *Proceedings of the National Academy of Sciences* **2007**, *104*, 17370-17375.
(42) Annibale, P.; Vanni, S.; Scarselli, M.; Rothlisberger, U.; Radenovic, A. *PLOS ONE* **2011**, *6*, e22678.
(43) Gabor, K. A.; Stevens, C. R.; Pietraszewski, M. J.; Gould, T. J.; Shim, J.; Yoder, J. A.; Lam, S. H.; Gong, Z.; Hess, S. T.; Kim, C. H. *PLOS ONE* **2013**, *8*, e68759.
(44) Sherman, E.; Barr, V.; Manley, S.; Patterson, G.; Balagopalan, L.; Akpan, I.; Regan, Carole K.; Merrill, Robert K.; Sommers, Connie L.; Lippincott-Schwartz, J.; Samelson, Lawrence E. *Immunity* **2011**, *35*, 705-720.
(45) Tobin, S. J.; Cacao, E. E.; Hong, D. W. W.; Terenius, L.; Vukojevic, V.; Jovanovic-Talisman, T. *PLOS ONE* **2014**, *9*, e87225.
(46) Manley, S.; Gillette, J. M.; Patterson, G. H.; Shroff, H.; Hess, H. F.; Betzig, E.; Lippincott-Schwartz, J. *Nature Methods* **2008**, *5*, 155-157.
(47) Heidbreder, M.; Zander, C.; Malkusch, S.; Widera, D.; Kaltschmidt, B.; Kaltschmidt, C.; Nair, D.; Choquet, D.; Sibarita, J.-B.; Heilemann, M. *Biochimica et Biophysica Acta (BBA) - Molecular Cell Research* **2012**, *1823*, 1984-1989.
(48) Shrivastava, A.; Rodriguez, P.; Triller, A.; Renner, M. *Frontiers in Cellular Neuroscience* **2013**, *7*, 1-11.
(49) Subach, F. V.; Patterson, G. H.; Renz, M.; Lippincott-Schwartz, J.; Verkhusha, V. V. *Journal of the American Chemical Society* **2010**, *132*, 6481-6491.
(50) Dudok, B.; Barna, L.; Ledri, M.; Szabó, S. I.; Szabadits, E.; Pintér, B.; Woodhams, S. G.; Henstridge, C. M.; Balla, G. Y.; Nyilas, R.; Varga, C.; Lee, S.-H.; Matolcsi, M.; Cervenak, J.;

Kacskovics, I.; Watanabe, M.; Sagheddu, C.; Melis, M.; Pistis, M.; Soltesz, I.; Katona, I. *Nature Neuroscience* **2014**, *18*, 75-76.
(51) Gao, J.; Wang, Y.; Cai, M.; Pan, Y.; Xu, H.; Jiang, J.; Ji, H.; Wang, H. *Nanoscale* **2015**, *7*, 2511-2519.
(52) Hartley, J. M.; Chu, T.-W.; Peterson, E. M.; Zhang, R.; Yang, J.; Harris, J.; Kopeček, J. *ChemBioChem* **2015**, *16*, 1725-1729.
(53) Lee, J.; Sengupta, P.; Brzostowski, J.; Lippincott-Schwartz, J.; Pierce, S. K.; Lidke, D. *Molecular Biology of the Cell* **2017**, *28*, 511-523.
(54) Lee, S. F.; Vérolet, Q.; Fürstenberg, A. *Angewandte Chemie International Edition* **2013**, *52*, 8948-8951.
(55) Shelby, Sarah A.; Holowka, D.; Baird, B.; Veatch, Sarah L. *Biophysical Journal* **2013**, *105*, 2343-2354.
(56) Truan, Z.; Tarancón Díez, L.; Bönsch, C.; Malkusch, S.; Endesfelder, U.; Munteanu, M.; Hartley, O.; Heilemann, M.; Fürstenberg, A. *Journal of Structural Biology* **2013**, *184*, 329-334.
(57) Jiang, H.; English, B. P.; Hazan, R. B.; Wu, P.; Ovryn, B. *Angewandte Chemie International Edition* **2015**, *54*, 1765-1769.
(58) Letschert, S.; Göhler, A.; Franke, C.; Bertleff-Zieschang, N.; Memmel, E.; Doose, S.; Seibel, J.; Sauer, M. *Angewandte Chemie International Edition* **2014**, *53*, 10921-10924.
(59) Aaron, J. S.; Carson, B. D.; Timlin, J. A. *Small* **2012**, *8*, 3041-3049.
(60) Chen, J.; Gao, J.; Wu, J.; Zhang, M.; Cai, M.; Xu, H.; Jiang, J.; Tian, Z.; Wang, H. *Nanoscale* **2015**, *7*, 3373-3380.
(61) Maity, P. C.; Blount, A.; Jumaa, H.; Ronneberger, O.; Lillemeier, B. F.; Reth, M. *Science Signaling* **2015**, *8*, ra93, 1-15.
(62) Wang, J.; Richards, D. A. *Biology Open* **2012**, *1*, 857-862.
(63) Notelaers, K.; Rocha, S.; Paesen, R.; Swinnen, N.; Vangindertael, J.; Meier, J.; Rigo, J.-M.; Ameloot, M.; Hofkens, J. *Histochemistry & Cell Biology* **2014**, *142*, 79-90.
(64) Ji, C.; Zhang, Y.; Xu, P.; Xu, T.; Lou, X. *Journal of Biological Chemistry* **2015**, *290*, 26978-26993.
(65) Mattila, Pieta K.; Feest, C.; Depoil, D.; Treanor, B.; Montaner, B.; Otipoby, Kevin L.; Carter, R.; Justement, Louis B.; Bruckbauer, A.; Batista, Facundo D. *Immunity* **2013**, *38*, 461-474.

(66) Owen, D. M.; Rentero, C.; Rossy, J.; Magenau, A.; Williamson, D.; Rodriguez, M.; Gaus, K. *Journal of Biophotonics* **2010**, *3*, 446-454.
(67) Pageon, S. V.; Tabarin, T.; Yamamoto, Y.; Ma, Y.; Nicovich, P. R.; Bridgeman, J. S.; Cohnen, A.; Benzing, C.; Gao, Y.; Crowther, M. D.; Tungatt, K.; Dolton, G.; Sewell, A. K.; Price, D. A.; Acuto, O.; Parton, R. G.; Gooding, J. J.; Rossy, J.; Rossjohn, J.; Gaus, K. *Proceedings of the National Academy of Sciences* **2016**, *113*, E5454-E5463.
(68) Shelby, S. A.; Veatch, S. L.; Holowka, D. A.; Baird, B. A.; Lippincott-Schwartz, J. *Molecular Biology of the Cell* **2016**, *27*, 3645-3658.
(69) Stone, M. B.; Shelby, S. A.; Núñez, M. F.; Wisser, K.; Veatch, S. L. *eLife* **2017**, *6*, e19891.
(70) Stone, M. B.; Veatch, S. L. *Nature Communications* **2015**, *6*, 7347, 1-9.
(71) Williamson, D. J.; Owen, D. M.; Rossy, J.; Magenau, A.; Wehrmann, M.; Gooding, J. J.; Gaus, K. *Nature Immunology* **2011**, *12*, 655-663.
(72) Bernhem, K.; Blom, H.; Brismar, H. *PLoS One* **2018**, *13*, e0195825.
(73) Liu, Q.; Chen, L.; Aguilar, H. C.; Chou, K. C. *Nat Commun* **2018**, *9*, 3050, 1-7.
(74) Jonas, K. C.; Fanelli, F.; Huhtaniemi, I. T.; Hanyaloglu, A. C. *Journal of Biological Chemistry* **2015**, *290*, 3875-3892.
(75) Peterson, J. A.; Wijesooriya, C.; Gehrmann, E. J.; Mahoney, K. M.; Goswami, P. P.; Albright, T. R.; Syed, A.; Dutton, A. S.; Smith, E. A.; Winter, A. H. *Journal of the American Chemical Society* **2018**, *140*, 7343-7346.
(76) He, H.; Liu, X.; Li, S.; Wang, X.; Wang, Q.; Li, J.; Wang, J.; Ren, H.; Ge, B.; Wang, S.; Zhang, X.; Huang, F. *Anal Chem* **2017**, *89*, 11831-11838.
(77) Sharonov, A.; Hochstrasser, R. M. *Proceedings of the National Academy of Sciences* **2006**, *103*, 18911-18916.
(78) Giannone, G.; Hosy, E.; Levet, F.; Constals, A.; Schulze, K.; Sobolevsky, Alexander I.; Rosconi, M. P.; Gouaux, E.; Tampé, R.; Choquet, D.; Cognet, L. *Biophysical Journal* **2010**, *99*, 1303-1310.
(79) Winckler, P.; Lartigue, L.; Giannone, G.; De Giorgi, F.; Ichas, F.; Sibarita, J.-B.; Lounis, B.; Cognet, L. *Scientific Reports* **2013**, *3*, 2387, 1-5.
(80) Jungmann, R.; Steinhauer, C.; Scheible, M.; Kuzyk, A.; Tinnefeld, P.; Simmel, F. C. *Nano Letters* **2010**, *10*, 4756-4761.

(81) Schnitzbauer, J.; Strauss, M. T.; Schlichthaerle, T.; Schueder, F.; Jungmann, R. *Nature Protocols* **2017**, *12*, 1198-1228.
(82) Jayasinghe, I.; Clowsley, A. H.; Lin, R. S.; Lutz, T.; Harrison, C.; Green, E.; Baddeley, D.; Di Michele, L.; Soeller, C. *Cell Rep* **2018**, *22*, 557-567.
(83) Werbin, J. L.; Avendaño, M. S.; Becker, V.; Jungmann, R.; Yin, P.; Danuser, G.; Sorger, P. K. *Scientific Reports* **2017**, *7*, 12150, 1-12.
(84) Burgert, A.; Letschert, S.; Doose, S.; Sauer, M. *Histochemistry and Cell Biology* **2015**, *144*, 123-131.
(85) Dertinger, T.; Colyer, R.; Iyer, G.; Weiss, S.; Enderlein, J. *Proceedings of the National Academy of Sciences* **2009**, *106*, 22287-22292.
(86) Deschout, H.; Lukes, T.; Sharipov, A.; Szlag, D.; Feletti, L.; Vandenberg, W.; Dedecker, P.; Hofkens, J.; Leutenegger, M.; Lasser, T.; Radenovic, A. *Nature Communications* **2016**, *7*, 13693, 1-11.
(87) Geissbuehler, S.; Dellagiacoma, C.; Lasser, T. *Biomed. Opt. Express* **2011**, *2*, 408-420.
(88) Dertinger, T.; Colyer, R.; Vogel, R.; Enderlein, J.; Weiss, S. *Opt. Express* **2010**, *18*, 18875-18885.
(89) Geissbuehler, S.; Bocchio, N. L.; Dellagiacoma, C.; Berclaz, C.; Leutenegger, M.; Lasser, T. *Optical Nanoscopy* **2012**, *1*, 4, 1-7.
(90) Lukeš, T.; Glatzová, D.; Kvíčalová, Z.; Levet, F.; Benda, A.; Letschert, S.; Sauer, M.; Brdička, T.; Lasser, T.; Cebecauer, M. *Nature Communications* **2017**, *8*, 1731, 1-7.
(91) Dedecker, P.; Mo, G. C.; Dertinger, T.; Zhang, J. *Proc Natl Acad Sci U S A* **2012**, *109*, 10909-10914.
(92) Mo, G. C.; Ross, B.; Hertel, F.; Manna, P.; Yang, X.; Greenwald, E.; Booth, C.; Plummer, A. M.; Tenner, B.; Chen, Z.; Wang, Y.; Kennedy, E. J.; Cole, P. A.; Fleming, K. G.; Palmer, A.; Jimenez, R.; Xiao, J.; Dedecker, P.; Zhang, J. *Nat Methods* **2017**, *14*, 427-434.
(93) Hell, S. W.; Wichmann, J. *Opt Lett* **1994**, *19*, 780-782.
(94) Gao, M.; Maraspini, R.; Beutel, O.; Zehtabian, A.; Eickholt, B.; Honigmann, A.; Ewers, H. *ACS Nano* **2018**, *12*, 4178-4185.
(95) Rittweger, E.; Han, K. Y.; Irvine, S. E.; Eggeling, C.; Hell, S. W. *Nature Photonics* **2009**, *3*, 144-147.

(96) Wildanger, D.; Patton, B. R.; Schill, H.; Marseglia, L.; Hadden, J. P.; Knauer, S.; Schönle, A.; Rarity, J. G.; O'Brien, J. L.; Hell, S. W.; Smith, J. M. *Advanced Materials* **2012**, *24*, OP309-OP313.
(97) Arlt, J.; Padgett, M. J. *Opt. Lett.* **2000**, *25*, 191-193.
(98) Dyba, M.; Hell, S. W. *Physical review letters* **2002**, *88*, 163901.
(99) Friedrich, M.; Gan, Q.; Ermolayev, V.; Harms, Gregory S. *Biophysical Journal* **2011**, *100*, L43-L45.
(100) Blom, H.; Widengren, J. *Chemical Reviews* **2017**, *117*, 7377-7427.
(101) Vicidomini, G.; Bianchini, P.; Diaspro, A. *Nature Methods* **2018**, *15*, 173-182.
(102) Roobala, C.; Ilanila, I. P.; Basu, J. K. *J Biosciences* **2018**, *43*, 471-484.
(103) Milovanovic, D.; Honigmann, A.; Koike, S.; Göttfert, F.; Pähler, G.; Junius, M.; Müllar, S.; Diederichsen, U.; Janshoff, A.; Grubmüller, H.; Risselada, H. J.; Eggeling, C.; Hell, S. W.; van den Bogaart, G.; Jahn, R. *Nature Communications* **2015**, *6*, 5984, 1-10.
(104) Sieber, J. J.; Willig, K. I.; Heintzmann, R.; Hell, S. W.; Lang, T. *Biophysical Journal* **2006**, *90*, 2843-2851.
(105) Sieber, J. J.; Willig, K. I.; Kutzner, C.; Gerding-Reimers, C.; Harke, B.; Donnert, G.; Rammner, B.; Eggeling, C.; Hell, S. W.; Grubmüller, H.; Lang, T. *Science* **2007**, *317*, 1072-1076.
(106) van den Bogaart, G.; Meyenberg, K.; Risselada, H. J.; Amin, H.; Willig, K. I.; Hubrich, B. E.; Dier, M.; Hell, S. W.; Grubmüller, H.; Diederichsen, U.; Jahn, R. *Nature* **2011**, *479*, 552-555.
(107) Blom, H.; Rönnlund, D.; Scott, L.; Spicarova, Z.; Widengren, J.; Bondar, A.; Aperia, A.; Brismar, H. *BMC Neuroscience* **2011**, *12*, 16, 1-7.
(108) Willig, K. I.; Rizzoli, S. O.; Westphal, V.; Jahn, R.; Hell, S. W. *Nature* **2006**, *440*, 935-939.
(109) Mazkereth, N.; Rocca, F.; Schubert, J.-R.; Geisler, C.; Hillman, Y.; Egner, A.; Fishelson, Z. *Immunobiology* **2016**, *221*, 1395-1406.
(110) Shin, W.; Ge, L.; Arpino, G.; Villarreal, S. A.; Hamid, E.; Liu, H.; Zhao, W.-D.; Wen, P. J.; Chiang, H.-C.; Wu, L.-G. *Cell* **2018**, *173*, 934-945.
(111) de Coninck, D.; Schmidt, T. H.; Schloetel, J. G.; Lang, T. *Biophys J* **2018**, *114*, 1128-1141.
(112) Merklinger, E.; Schloetel, J. G.; Weber, P.; Batoulis, H.; Holz, S.; Karnowski, N.; Finke, J.; Lang, T. *Elife* **2017**, *6*, e20705.

(113) Sarangi, N. K.; Roobala, C.; Basu, J. K. *Methods* **2018**, *140-141*, 198-211.
(114) Clausen, M. P.; Sezgin, E.; Bernardino de la Serna, J.; Waithe, D.; Lagerholm, B. C.; Eggeling, C. *Methods* **2015**, *88*, 67-75.
(115) Schneider, F.; Waithe, D.; Clausen, M. P.; Galiani, S.; Koller, T.; Ozhan, G.; Eggeling, C.; Sezgin, E. *Mol Biol Cell* **2017**, *28*, 1507-1518.
(116) Bianchini, P.; Cardarelli, F.; Luca, M. D.; Diaspro, A.; Bizzarri, R. *PLOS ONE* **2014**, *9*, e99619.
(117) Benda, A.; Ma, Y.; Gaus, K. *Biophys J* **2015**, *108*, 596-609.
(118) Honigmann, A.; Mueller, V.; Ta, H.; Schoenle, A.; Sezgin, E.; Hell, S. W.; Eggeling, C. *Nat Commun* **2014**, *5*, 5412, 1-12.
(119) Maraspini, R.; Beutel, O.; Honigmann, A. *Methods* **2018**, *140-141*, 188-197.
(120) Heintzmann, R.; Huser, T. *Chemical Reviews* **2017**, *117*, 13890-13908.
(121) Ashdown, G. W.; Burn, G. L.; Williamson, D. J.; Pandžić, E.; Peters, R.; Holden, M.; Ewers, H.; Shao, L.; Wiseman, P. W.; Owen, D. M. *Biophysical Journal* **2017**, *112*, 1703-1713.
(122) Bridges, A. A.; Jentzsch, M. S.; Oakes, P. W.; Occhipinti, P.; Gladfelter, A. S. *The Journal of Cell Biology* **2016**, *213*, 23-32.
(123) Brown, A. C.; Oddos, S.; Dobbie, I. M.; Alakoskela, J. M.; Parton, R. M.; Eissmann, P.; Neil, M. A.; Dunsby, C.; French, P. M.; Davis, I.; Davis, D. M. *PLoS Biol* **2011**, *9*, e1001152.
(124) Brown, A. C. N.; Dobbie, I. M.; Alakoskela, J.-M.; Davis, I.; Davis, D. M. *Blood* **2012**, *120*, 3729-3740.
(125) Ashdown, G. W.; Owen, D. M. *Methods* **2018**, *140-141*, 112-118.
(126) Hu, Y. S.; Cang, H.; Lillemeier, B. F. *Proceedings of the National Academy of Sciences* **2016**, *113*, 7201-7206.
(127) York, A. L.; Zheng, J. Q. *eneuro* **2017**, *4*, e0232-17.
(128) Curd, A.; Cleasby, A.; Makowska, K.; York, A.; Shroff, H.; Peckham, M. *Methods* **2015**, *88*, 37-47.
(129) Guo, M.; Chandris, P.; Giannini, J. P.; Trexler, A. J.; Fischer, R.; Chen, J.; Vishwasrao, H. D.; Rey-Suarez, I.; Wu, Y.; Wu, X.; Waterman, C. M.; Patterson, G. H.; Upadhyaya, A.; Taraska, J. W.; Shroff, H. *Nature Methods* **2018**, *15*, 425-428.
(130) Wang, H. Y.; Sun, J.; Xia, L. Y.; Li, Y. H.; Chen, Z.; Wu, F. G. *Acs Biomaterials Science & Engineering* **2017**, *3*, 2570-2578.

(131) Kilin, V.; Glushonkov, O.; Herdly, L.; Klymchenko, A.; Richert, L.; Mely, Y. *Biophys J* **2015**, *108*, 2521-2531.
(132) Wang, H.; Feng, Z.; Del Signore, S. J.; Rodal, A. A.; Xu, B. *J Am Chem Soc* **2018**, *140*, 3505-3509.
(133) Zhang, X.; Wang, B.; Xiao, Y.; Wang, C.; He, L. *Analyst* **2018**, *143*, 4180-4188.
(134) Jiao, Y.; Yin, J.; He, H.; Peng, X.; Gao, Q.; Duan, C. *J Am Chem Soc* **2018**, *140*, 5882-5885.
(135) Hirata, T.; Terai, T.; Yamamura, H.; Shimonishi, M.; Komatsu, T.; Hanaoka, K.; Ueno, T.; Imaizumi, Y.; Nagano, T.; Urano, Y. *Anal Chem* **2016**, *88*, 2693-2700.
(136) Li, M.; Nie, C.; Feng, L.; Yuan, H.; Liu, L.; Lv, F.; Wang, S. *Chemistry – An Asian Journal* **2014**, *9*, 3121-3124.
(137) Liu, P.; Li, S.; Jin, Y.; Qian, L.; Gao, N.; Yao, S. Q.; Huang, F.; Xu, Q.-H.; Cao, Y. *ACS Applied Materials & Interfaces* **2015**, *7*, 6754-6763.
(138) Huang, B.; Geng, Z.; Yan, S.; Li, Z.; Cai, J.; Wang, Z. *Anal Chem* **2017**, *89*, 8816-8821.
(139) Zhang, W.; Peng, B.; Tian, F.; Qin, W.; Qian, X. *Anal Chem* **2014**, *86*, 482-489.
(140) Gao, L.; Liu, M.; Ma, G.; Wang, Y.; Zhao, L.; Yuan, Q.; Gao, F.; Liu, R.; Zhai, J.; Chai, Z.; Zhao, Y.; Gao, X. *ACS Nano* **2015**, *9*, 10979-10990.
(141) Liu, A.; Peng, S.; Soo, J. C.; Kuang, M.; Chen, P.; Duan, H. *Anal Chem* **2011**, *83*, 1124-1130.
(142) Krafft, C.; Schmitt, M.; Schie, I. W.; Cialla-May, D.; Matthaus, C.; Bocklitz, T.; Popp, J. *Angew Chem Int Ed Engl* **2017**, *56*, 4392-4430.
(143) Syed, A.; Smith, E. A. *Annu Rev Anal Chem (Palo Alto Calif)* **2017**, *10*, 271-291.
(144) Zito, G.; Rusciano, G.; Pesce, G.; Dochshanov, A.; Sasso, A. *Nanoscale* **2015**, *7*, 8593-8606.
(145) Fogarty, S. W.; Patel, II; Martin, F. L.; Fullwood, N. J. *PLoS One* **2014**, *9*, e106283, 1-7.
(146) Yamaguchi, S.; Matsushita, T.; Izuta, S.; Katada, S.; Ura, M.; Ikeda, T.; Hayashi, G.; Suzuki, Y.; Kobayashi, K.; Tokunaga, K.; Ozeki, Y.; Okamoto, A. *Sci Rep* **2017**, *7*, 41007, 1-7.
(147) Chen, Y.; Bai, X.; Su, L.; Du, Z.; Shen, A.; Materny, A.; Hu, J. *Sci Rep* **2016**, *6*, 19173, 1-12.
(148) Chen, Y.; Ren, J. Q.; Zhang, X. G.; Wu, D. Y.; Shen, A. G.; Hu, J. M. *Anal Chem* **2016**, *88*, 6115-6119.

(149) Chen, H. K.; Wang, S. Q.; Zhang, Y. Q.; Yang, Y.; Fang, H.; Zhu, S. W.; Yuan, X. C. *Opt Commun* **2017**, *402*, 221-225.
(150) Etchegoin, P. G.; Lacharmoise, P. D.; Le Ru, E. C. *Anal Chem* **2009**, *81*, 682-688.
(151) Kudelski, A.; Pettinger, B. *Chem Phys Lett* **2000**, *321*, 356-362.
(152) Zhang, W.; Cui, X.; Yeo, B. S.; Schmid, T.; Hafner, C.; Zenobi, R. *Nano Lett* **2007**, *7*, 1401-1405.
(153) Wessel, J. *J. Opt. Soc. Am. B* **1985**, *2*, 1538-1541.
(154) Anderson, M. S. *Applied Physics Letters* **2000**, *76*, 3130-3132.
(155) Hayazawa, N.; Inouye, Y.; Sekkat, Z.; Kawata, S. *Opt Commun* **2000**, *183*, 333-336.
(156) Pettinger, B. P., G.; Schuster, R.; Ertl, G. . *Electrochemistry* **2000**, *68*, 942-949.
(157) Stockle, R. M. S., Y. D.; Deckert, V.; Zenobi, R. . *Chem Phys Lett* **2000**, *318*, 131-136.
(158) Kurouski, D.; Deckert-Gaudig, T.; Deckert, V.; Lednev, I. K. *Journal of the American Chemical Society* **2012**, *134*, 13323-13329.
(159) Liao, M.; Jiang, S.; Hu, C.; Zhang, R.; Kuang, Y.; Zhu, J.; Zhang, Y.; Dong, Z. *Nano Letters* **2016**, *16*, 4040-4046.
(160) Zhang, R.; Zhang, Y.; Dong, Z. C.; Jiang, S.; Zhang, C.; Chen, L. G.; Zhang, L.; Liao, Y.; Aizpurua, J.; Luo, Y.; Yang, J. L.; Hou, J. G. *Nature* **2013**, *498*, 82-86.
(161) Gao, L.; Zhao, H.; Li, T.; Huo, P.; Chen, D.; Liu, B. *International Journal of Molecular Sciences* **2018**, *19*, 1193, DOI:10.3390/ijms19041193.
(162) Kurouski, D. *Vibrational Spectroscopy* **2017**, *91*, 3-15.
(163) Schmid, T.; Opilik, L.; Blum, C.; Zenobi, R. *Angewandte Chemie International Edition* **2013**, *52*, 5940-5954.
(164) Xiao, L.; Schultz, Z. D. *Analytical Chemistry* **2018**, *90*, 440-458.
(165) Zhang, Z.; Sheng, S.; Wang, R.; Sun, M. *Analytical Chemistry* **2016**, *88*, 9328-9346.
(166) Böhme, R.; Cialla, D.; Richter, M.; Rösch, P.; Popp, J.; Deckert, V. *Journal of Biophotonics* **2010**, *3*, 455-461.
(167) Böhme, R.; Richter, M.; Cialla, D.; Rösch, P.; Deckert, V.; Popp, J. *Journal of Raman Spectroscopy* **2009**, *40*, 1452-1457.
(168) Nakata, A.; Nomoto, T.; Toyota, T.; Fujinami, M. *Analytical Sciences* **2013**, *29*, 865-869.
(169) Opilik, L.; Bauer, T.; Schmid, T.; Stadler, J.; Zenobi, R. *Physical Chemistry Chemical Physics* **2011**, *13*, 9978-9981.

(170) Neugebauer, U.; Rösch, P.; Schmitt, M.; Popp, J.; Julien, C.; Rasmussen, A.; Budich, C.; Deckert, V. *ChemPhysChem* **2006**, *7*, 1428-1430.
(171) Neugebauer, U.; Schmid, U.; Baumann, K.; Ziebuhr, W.; Kozitskaya, S.; Deckert, V.; Schmitt, M.; Popp, J. *ChemPhysChem* **2007**, *8*, 124-137.
(172) Cialla, D.; Deckert-Gaudig, T.; Budich, C.; Laue, M.; Möller, R.; Naumann, D.; Deckert, V.; Popp, J. *Journal of Raman Spectroscopy* **2009**, *40*, 240-243.
(173) Hermann, P.; Hermelink, A.; Lausch, V.; Holland, G.; Möller, L.; Bannert, N.; Naumann, D. *Analyst* **2011**, *136*, 1148-1152.
(174) Olschewski, K.; Kämmer, E.; Stöckel, S.; Bocklitz, T.; Deckert-Gaudig, T.; Zell, R.; Cialla-May, D.; Weber, K.; Deckert, V.; Popp, J. *Nanoscale* **2015**, *7*, 4545-4552.
(175) Berezin, S.; Aviv, Y.; Aviv, H.; Goldberg, E.; Tischler, Y. R. *Scientific Reports* **2017**, *7*, 3810, DOI:10.1038/s41598-017-02212-2.
(176) Richter, M.; Hedegaard, M.; Deckert-Gaudig, T.; Lampen, P.; Deckert, V. *Small* **2011**, *7*, 209-214.
(177) Alexander, K. D.; Schultz, Z. D. *Analytical Chemistry* **2012**, *84*, 7408-7414.
(178) Wang, H.; Schultz , Z. D. *ChemPhysChem* **2014**, *15*, 3944-3949.
(179) Xiao, L.; Wang, H.; Schultz, Z. D. *Anal Chem* **2016**, *88*, 6547-6553.
(180) Martín Sabanés, N.; Driessen, L. M. A.; Domke, K. F. *Analytical Chemistry* **2016**, *88*, 7108-7114.
(181) Pienpinijtham, P.; Vantasin, S.; Kitahama, Y.; Ekgasit, S.; Ozaki, Y. *The Journal of Physical Chemistry C* **2016**, *120*, 14663-14668.
(182) Touzalin, T.; Dauphin, A. L.; Joiret, S.; Lucas, I. T.; Maisonhaute, E. *Physical Chemistry Chemical Physics* **2016**, *18*, 15510-15513.
(183) Klingsporn, J. M.; Sonntag, M. D.; Seideman, T.; Van Duyne, R. P. *The Journal of Physical Chemistry Letters* **2014**, *5*, 106-110.
(184) Silva, W. R.; Graefe, C. T.; Frontiera, R. R. *ACS Photonics* **2016**, *3*, 79-86.
(185) Ikeshoji, T.; Ono, Y.; Mizuno, T. *Appl. Opt.* **1973**, *12*, 2236-2237.
(186) Lesoine, M. D.; Bobbitt, J. M.; Zhu, S.; Fang, N.; Smith, E. A. *Analytica Chimica Acta* **2014**, *848*, 61-66.
(187) McKee, K. J.; Meyer, M. W.; Smith, E. A. *Analytical Chemistry* **2012**, *84*, 9049-9055.
(188) McKee, K. J.; Meyer, M. W.; Smith, E. A. *Analytical Chemistry* **2012**, *84*, 4300-4306.

(189) Nyamekye, C. K. A.; Weibel, S. C.; Bobbitt, J. M.; Smith, E. A. *Analyst* **2018**, *143*, 400-408.

(190) McKee, K. J.; Smith, E. A. *Review of Scientific Instruments* **2010**, *81*, 043106, 1-6.

(191) M., B. J.; A., S. E. *Journal of Raman Spectroscopy* **2018**, *49*, 262-270.

(192) Iwamoto, R.; Ohta, K.; Miya, M.; Mima, S. *Appl. Spectrosc.* **1981**, *35*, 584-587.

(193) Lee, C.; Bain, C. D. *Biochimica et Biophysica Acta (BBA) - Biomembranes* **2005**, *1711*, 59-71.

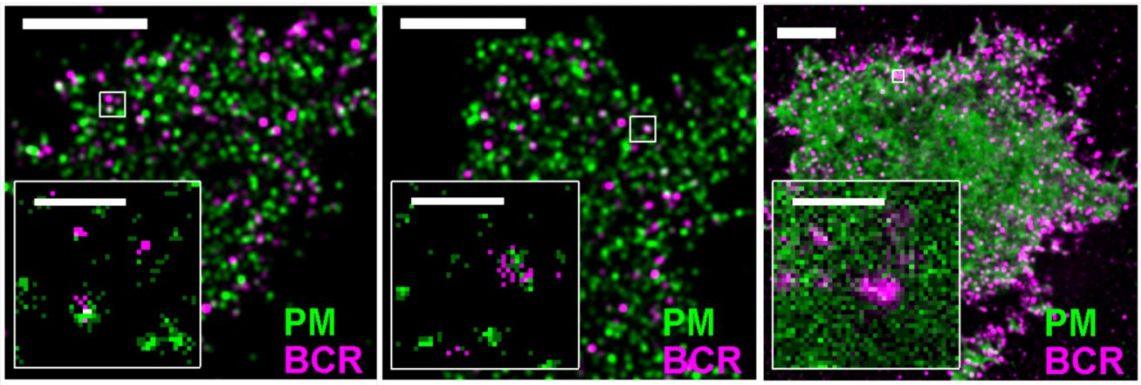

Figure 1. Two-color SMLM images collected using a combination of PALM and STORM showing the colocalization of B cell receptor clusters (magenta color) within ordered membrane domains (green color) in CH27 B cells. Images were collected using cells fixed (left) one minute or (middle) five minutes after receptor clustering and (right) live cells. The receptor was labeled with an organic fluorophore, and receptors were clustered with a biotinylated antibody followed by (multivalent) streptavidin binding. Ordered membrane domains were labeled with lipidated peptide anchored to the inner membrane leaflet (PM peptide) and mEos3.2 fluorescent protein. Cross-correlation analysis was used to show colocalization. Reproduced from: Stone, M. B.; Shelby, S. A.; Núñez, M. F.; Wisser, K.; Veatch, S. L. Protein sorting by lipid phase-like domains supports emergent signaling function in B lymphocyte plasma membranes. eLife 2017, 6, e19891 (ref 69).

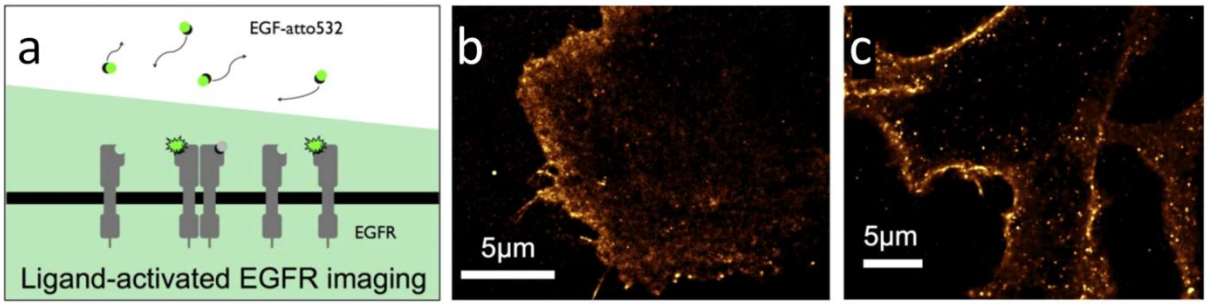

Figure 2. uPAINT super resolution images of endogenous epidermal growth factor receptor (EGFR) in COS7 plasma membranes. (a) Schematic showing the principle behind signal generation from the stochastic binding and unbinding of a fluorescent species. Reconstructed images from (b) 1.6×10^5 localizations with simultaneous incubation with 0.4 nM EGF-Atto 532 ligand (shown in the schematic) or (c) fluorescently-labeled ligand-binding-inhibitor panitumumab-Atto 647N. The illumination thickness is approximately two microns.

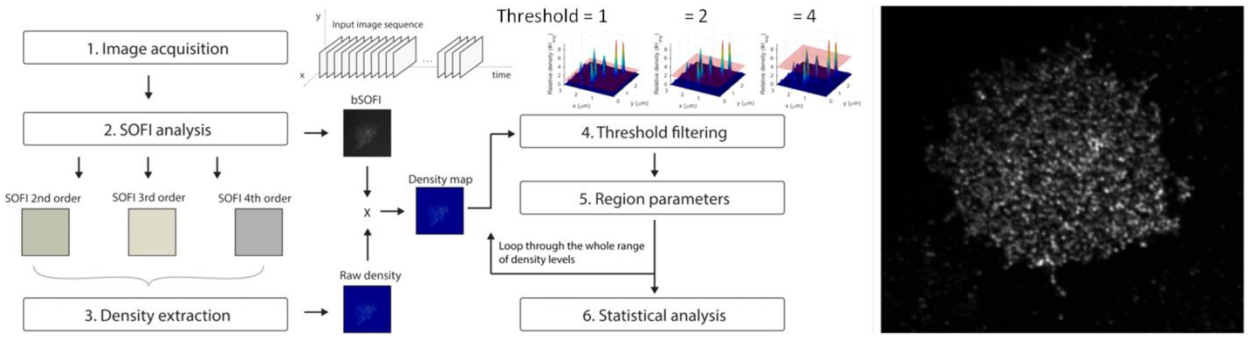

Figure 3. Representative steps in balanced SOFI data analysis using higher order statistics. First, a series of images of stochastically switching emitters is acquired in a similar fashion to SMLM experiments. The images are corrected for drift, for example using gold nanoparticle fiducial markers, which is problematic for super resolution imaging techniques that require collecting data over time with a microscope. The series of images is then divided into sub-series, each with a smaller number of frames than the total, which is necessary to account for photobleaching in the subsequent analysis. The SOFI analysis defines 2nd order and higher cumulants for each sub-series, the cumulants are averaged across each sub-series, and the averages are used to generate density maps that show the number of emitting fluorophores per pixel. Thresholds are applied to the density maps, and then regions of interest are analyzed for each threshold to define the number of "high density regions". The resultant image does not contain background and has a reduced noise level. The spatial resolution depends on the highest order cumulant, which can be increased with a larger data series consisting of more images (at the expense of collection time and additional photobleaching). At right is a bSOFI image collected with total internal reflection (TIRF) illumination showing CD4-mEos2 fusion protein clustering in a Jurkat T cell. Reprinted with modifications by permission from Macmillan Publishers Ltd: NATURE COMMUNICATIONS, Lukeš, T.; Glatzová, D.; Kvíčalová, Z.; Levet, F.; Benda, A.; Letschert, S.; Sauer, M.; Brdička, T.; Lasser, T.; Cebecauer, M., Nature Communications 2017, 8, 1731, 1-7 (ref # 90). Copyright 2017.

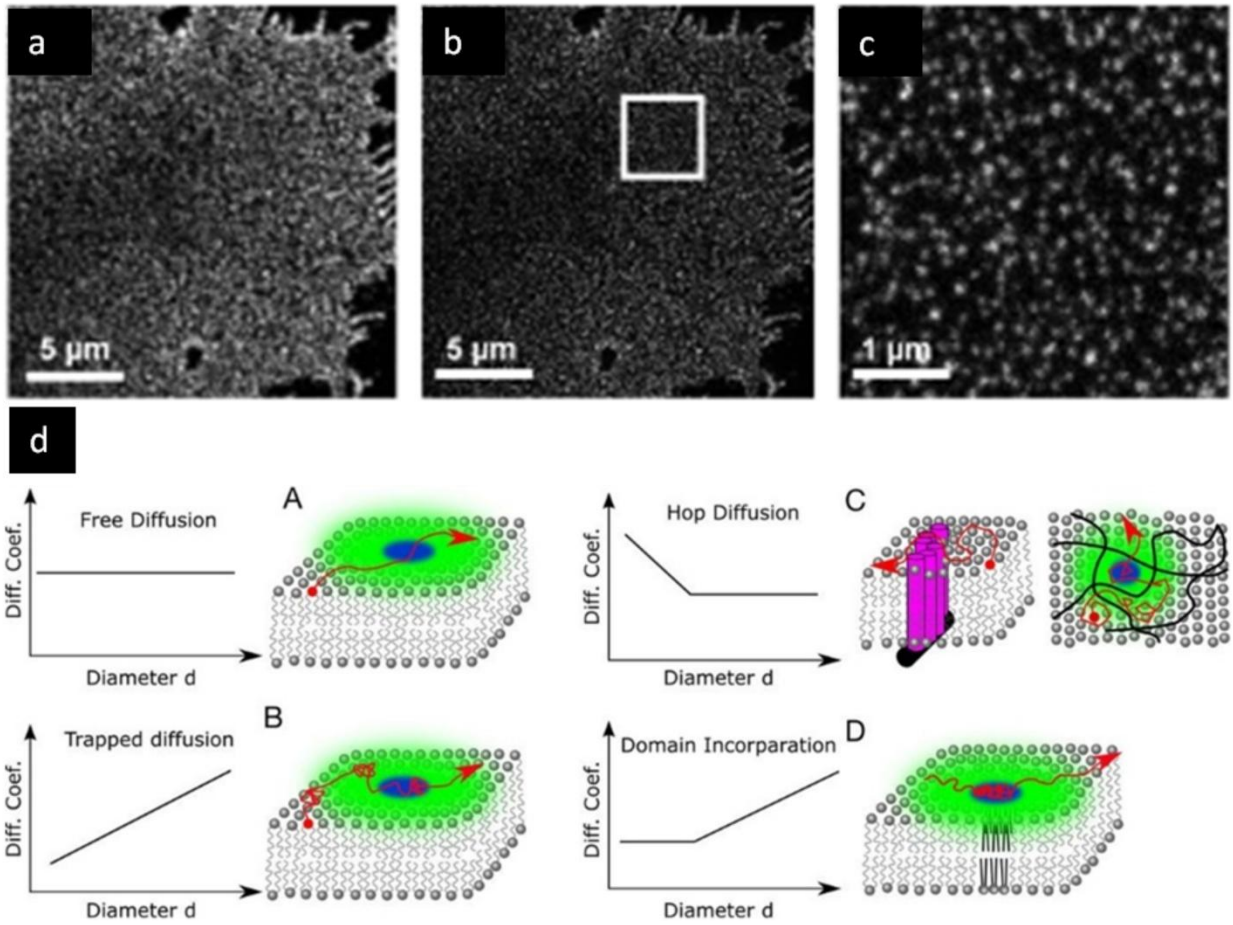

Figure 4. Examples of how STED can be used to measure (top) nanoscale organization of membrane components and (bottom) nanoscale dynamics. Syntaxin clusters imaged in the cell membrane of HepG2 cells using (a) confocal and (b) STED microscopy. Syntaxin is a SNARE protein that plays a role in vesicle fusion. (c) Magnified area of the white boxed area in image b. Reproduced from: Merklinger, E.; Schloetel, J. G.; Weber, P.; Batoulis, H.; Holz, S.; Karnowski, N.; Finke, J.; Lang, T. The packing density of a supramolecular membrane protein cluster is controlled by cytoplasmic interactions. eLife 2017, 6, e20705 (ref 112). (d) Information about membrane dynamics can be measured using STED FCS wherein a region represented by the blue circle is analyzed. STED FCS reveals details about modes of membrane diffusion that are averaged or not measured by confocal imaging using a diffraction-limited imaging area represented by the green circle. When the diffusion coefficient is measured across analysis regions of varying size (i.e., diameters), Brownian "free" diffusion can be differentiated from diffusion associated with a transient immobile or slow species, hop diffusion that may result from, for example, cytoskeleton-anchored

membrane components that form compartments represented by the black lines, and localization into a nanodomain that may be formed from different membrane compositions. The small analysis areas that are required to differentiate these modes of diffusion are generally not achieved with diffraction-limited imaging techniques, but are generally achievable by STED. In STED FCS, the area of the analyzed region can be varied using different STED laser irradiances. Reproduced from: Schneider, F.; Waithe, D.; Clausen, M. P.; Galiani, S.; Koller, T.; Ozhan, G.; Eggeling, C.; Sezgin, E. Mol Biol Cell 2017, 28, 1507-1518 (ref 115).

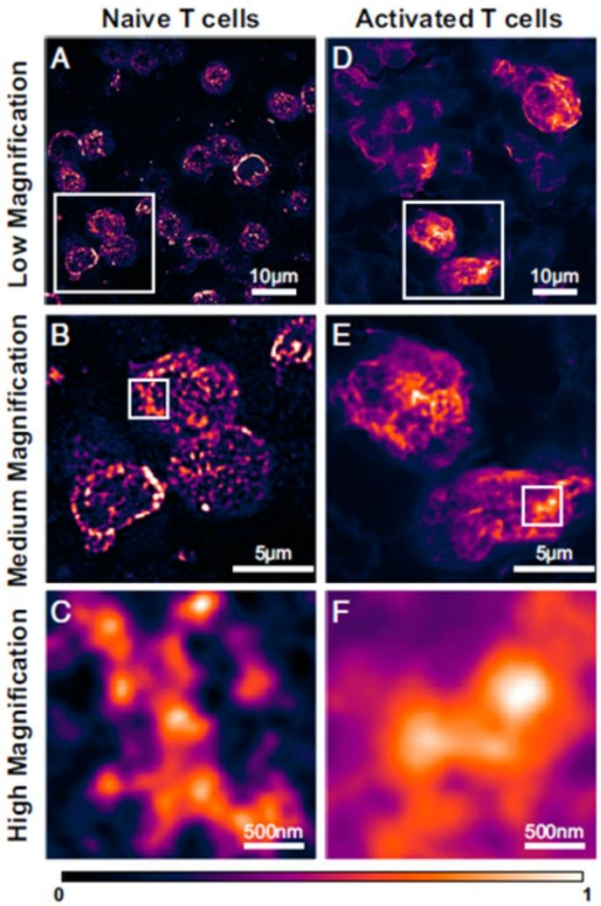

Figure 5. SIM images of the nanoscale distribution of the T-cell receptor in lymph-node-resident T cells. (A, B and C) before and (D, E and F) after in vivo T-cell activation. The images show that there is a change in the nanoscale organization after in vivo activation. B and E are magnified areas of the white boxes labeled in images A and D, respectively. Areas labeled with white boxes in B and E are enlarged in images C and F, respectively. The authors used SIM to ensure their reported SMLM images (specifically direct STORM) were not reporting artificial clusters, although the spatial resolution of the SIM images was not as good as what was achieved in dSTORM. Reproduced with permission from *Proceedings of the National Academy of Sciences USA* Hu, Y. S.; Cang, H.; Lillemeier, B. F. Proc. Natl. Acad. Sci. U.S.A. 2016, 113, 7201-7206 (ref # 126).

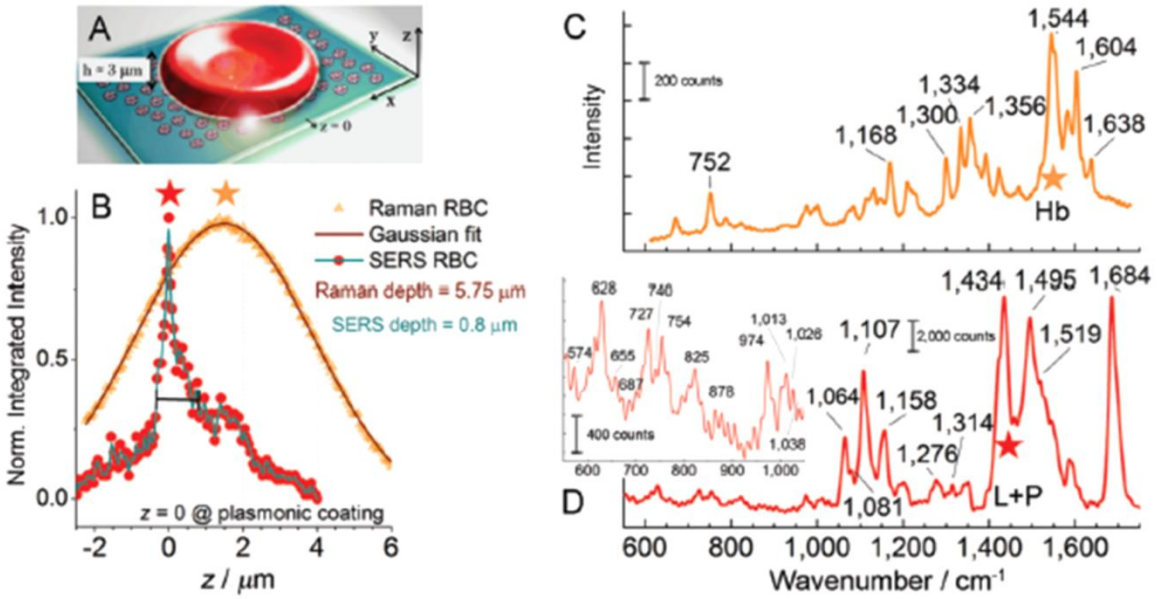

Figure 6. Membrane-selective SERS imaging is compared to confocal Raman imaging. (A) An inverted confocal microscope was used to collect the Raman signal from red blood cells coated on a glass substrate (confocal) or SERS substrate. (B) The SERS signal measures molecules with a 0.8 μm focal depth, and provided better axial resolution and selectivity for the cell membrane compared to confocal Raman imaging. (C) The confocal Raman spectrum has peaks that are characteristic of intracellular species (i.e., hemoglobin) whereas the (D) SERS spectrum shows peaks that are characteristic of membrane lipids and also proteins. The laser irradiance was approximately two orders of magnitude lower and the acquisition time was approximately ten-fold faster for the SERS measurement. Reproduced from Zito, G.; Rusciano, G.; Pesce, G.; Dochshanov, A.; Sasso, A. Nanoscale 2015, 7, 8593-8606 (ref 144), with permission of The Royal Society of Chemistry.

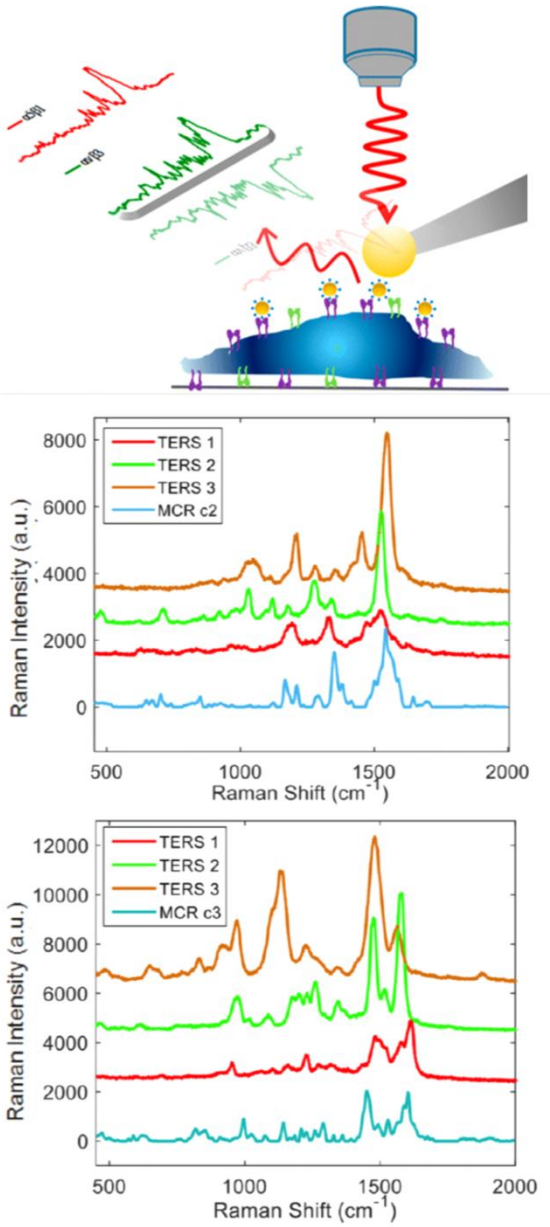

Figure 7. (Top) TERS measurements of two arginine-glycine-aspartate -binding integrin receptors (α5β1 and αvβ3) on fixed SW480 human colon cancer cells. The TERS tips consisted of cyclo-(arginine-glycine-aspartic acid-phenylalanine-cysteine)-coated gold nanoparticle to tag the integrin receptors. Integrins were identified using multivariant curve resolution (MCR) analysis. The middle panel of extracted spectra corresponds to α5β1 integrin and the bottom panel corresponds to αvβ3 integrin. Differences in the extracted spectra enable the selective imaging of these two different types of integrins. Reproduced from Xiao, L.; Wang, H.; Schultz, Z. D. *Anal Chem* **2016**, *88*, 6547-6553 (ref 179). Copyright 2016 American Chemical Society.

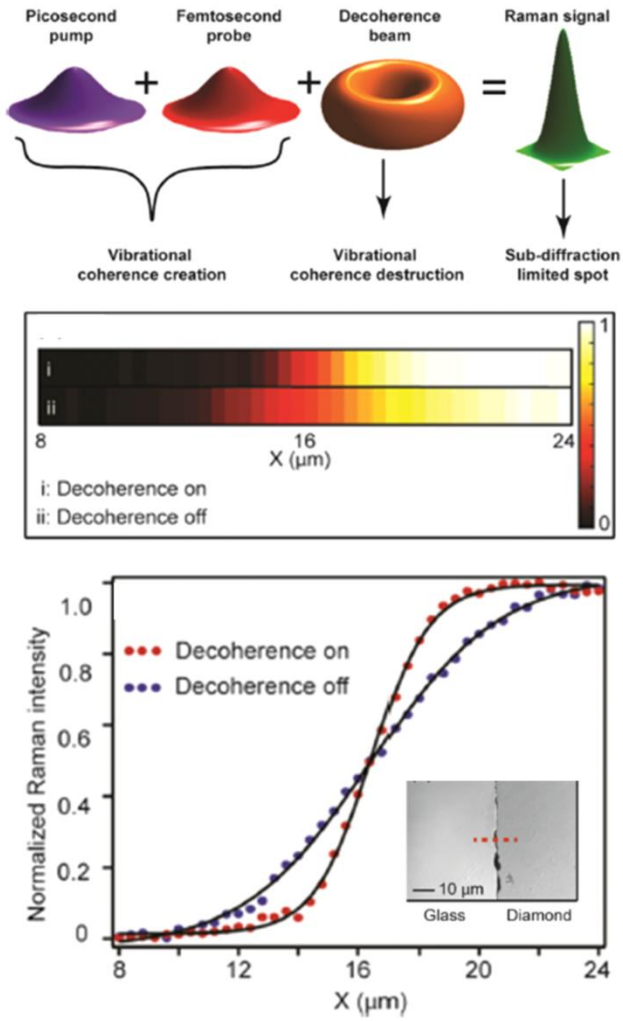

Figure 8. Femotsecond stimulated Raman spectroscopy (FSRS) imaging with a doughnut-shaped decoherence pulse to improve the spatial resolution. (Top) the picosecond pump and femtosecond probe pulses generate vibrational coherence and the FSRS signal. The coherence is removed around the periphery of the pump and probe pulses with a doughnut-shaped decoherence beam. The resulting FSRS signal is collected from a sub-diffraction region. (Middle) the collected Raman signal from a diamond sample with a step edge with the decoherence beam (i) on or (ii) off. The (bottom) image shows that the spatial resolution is improved when the decoherence beam is on. The inset shows an optical image of the diamond sample with the step edge. Reproduced from Silva, W. R.; Graefe, C. T.; Frontiera, R. R. ACS Photonics 2016, 3, 79-86 (ref 184). Copyright 2016 American Chemical Society.

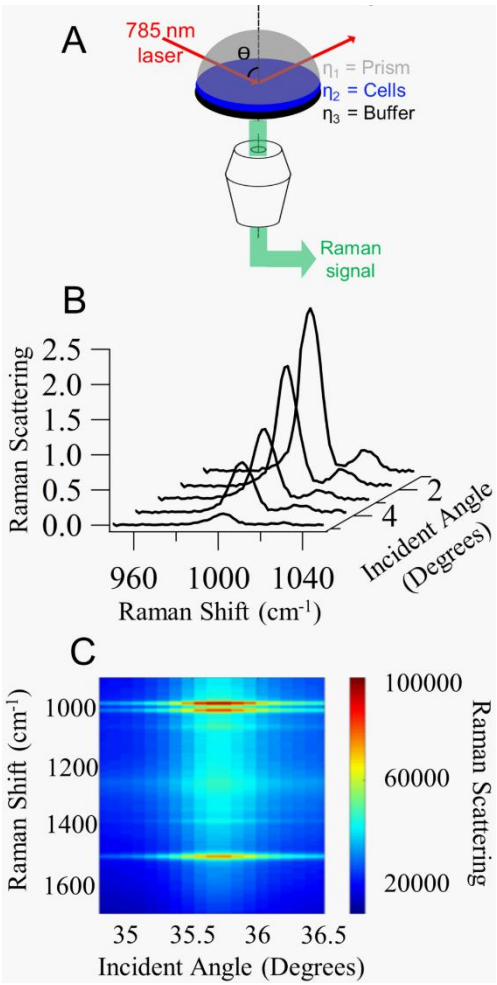

Figure 9. (A) A representative experimental setup of the total internal reflection illumination geometry wherein a laser propagates through a high refractive index material (η_1) to a lower refractive index material (η_2/η_3) at an angle greater than the critical angle. Using a prism/sample interface allows a larger range of incident angles to be achieved compared to sending the laser through the microscope objective off the optical axis. Under total internal reflection conditions, Raman scattering is generated from molecules located within the evanescent wave that is confined to approximately the wavelength of light or less from the prism interface. (B) In scanning angle Raman imaging, the incident angle (θ) of light is scanned at angles above the critical angle while simultaneously collecting the Raman spectra. Different axial thicknesses can be measured by scanning the incident angle of light, as demonstrated using a homogenous solution of benzonitrile to acquire Raman spectra at selected incident angles: (1) 37.47°, (2) 38.43°, (3) 41.31°, (4) 42.67°, and (5) 58.67°. With increasing incident angle, the Raman signal decreases due to the reduced volume over which the signal is collected from the homogeneous

sample. Reprinted from McKee, K. J.; Smith, E. A., Review of Scientific Instruments 2010, 81 (4), 043106 (ref 190), with the permission of AIP Publishing. (C) Plot of the Raman signal as a function of Raman shift and incident angle for a self-assembled monolayer of thiophenol adsorbed on smooth planar gold film. The maximum Raman scattering intensity is observed at the surface plasmon resonance angle (35.56°), where surface plasmons are generated in the metal film and the reflected light is maximally attenuated. Reproduced from Nyamekye, C. K. A.; Weibel, S. C.; Bobbitt, J. M.; Smith, E. A. Analyst 2018, 143 (2), 400-408 (ref 189), with permission of The Royal Society of Chemistry.

“for TOC only”

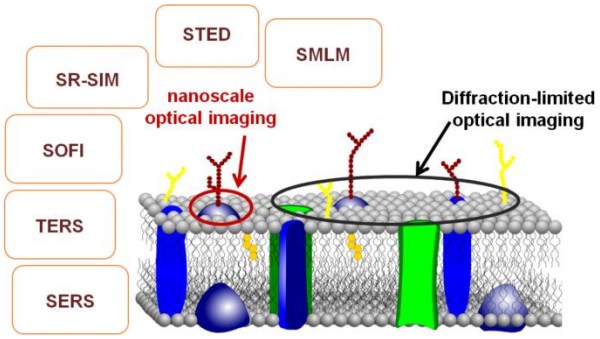
STED
SMLM
SR-SIM
nanoscale
optical imaging
Diffraction-limited
optical imaging
SOFI
TERS
SERS